

# Structure and optical properties of polymeric carbon nitrides from atomistic simulations

Changbin Im,<sup>†</sup> Björn Kirchoff,<sup>†</sup> Igor Krivtsov,<sup>‡</sup> Dariusz Mitoraj,<sup>†</sup> Radim Beranek,<sup>†</sup> and Timo Jacob<sup>\*,†,¶,§</sup>

<sup>†</sup>*Institute of Electrochemistry, Ulm University, Albert-Einstein-Allee 47, 89081 Ulm, Germany*

<sup>‡</sup>*Department of Organic and Inorganic Chemistry, University of Oviedo-CINN, 33006 Oviedo, Spain*

<sup>¶</sup>*Helmholtz-Institute-Ulm (HIU), Helmholtzstr. 11, 89081, Ulm, Germany*

<sup>§</sup>*Karlsruhe Institute of Technology (KIT), P.O. Box 3640, 76021, Karlsruhe, Germany*

E-mail: timo.jacob@uni-ulm.de

## Abstract

Detailed understanding of the structural and photophysical properties of polymeric carbon nitride (PCN) materials is of critical importance to derive future material optimization strategies towards more desirable optical properties and more photocatalytically active materials. However, the wide range of structural motifs found in synthesized PCNs complicates atomistic simulations that rely on well defined models. Performing hybrid DFT studies, we systematically investigate formation energy trends and optical properties of PCNs as a function of dimensionality, going from molecular oligomers over periodic sheet models to stacked crystals. Thermochemical calculations that take into account vibrational enthalpy and entropy contributions predict that a mixture of structural motifs including the melon string structure, poly(heptazine

imide), and g-C<sub>3</sub>N<sub>4</sub> motifs is stable under typical synthetic conditions. The degree of lateral condensation as well as stacking can reduce the bandgap while out-of-plane corrugation of the material increases both stability and the optical gap. The key result of this work is that already small domains of strongly condensed PCN are calculated to give rise to favorable optical properties. This result reconciles conflicting literature reports indicating that the thermodynamically favorable melon motif has a too large bandgap compared to experiments, while the g-C<sub>3</sub>N<sub>4</sub> structure, for which bandgap calculations are in better agreement with experiments, does not agree with measured chemical compositions of PCNs. Finally, we postulate a new computational model for carbon nitride materials that encompasses the most important structural motifs and shows a bandgap of *ca.* 2.9 eV.

## 1 Introduction

Polymeric carbon nitrides (PCNs) have recently gained considerable attention as a class of non-metallic photocatalytic materials.<sup>1</sup> Among many potential applications, this new material class is currently being explored in particular for photo-induced hydrogen production,<sup>2-7</sup> alcohol oxidation,<sup>8-11</sup> and the CO<sub>2</sub> reduction reaction<sup>12,13</sup> due to their intriguing photo-physical properties. PCNs feature optical gaps of *ca.* 2.8 eV.

Typical PCN materials obtained by straight-forward thermal synthesis are semi-crystalline and contain a multitude of micro-structural motifs.<sup>14-18</sup> This lack of crystallinity complicates structural characterization. However, if controlled reaction conditions can be enforced, certain motifs can become more prominent. For example, the "melon" structure, first described by Berzelius and Liebig<sup>19,20</sup> consisting of strands of linearly polycondensed melamine monomers interconnected via hydrogen bonds, was successfully synthesized by Lotsch *et al.* by thermal treatment of melamine in a closed reaction vessel at 630 °C.<sup>14,21,22</sup> A mesoporous, non-hydrogenated graphitic carbon nitride (g-C<sub>3</sub>N<sub>4</sub>) was postulated and explored for photocatalytic hydrogen production.<sup>23,24</sup> High condensation g-C<sub>3</sub>N<sub>4</sub> model systems, where

heptazine units are linked by tertiary amines into a 2D sheet structure, were suggested as theoretical models for PCNs by Lie and Cohen as early as 1989.<sup>25</sup> Since then, calculations explored models based on g-C<sub>3</sub>N<sub>4</sub> that exhibit desirable optical properties which are in good agreement with experimentally measured PCN samples.<sup>18</sup> However, the low hydrogen content of this structure is incompatible with elemental analysis of PCN samples, which are usually in better agreement with melon-type model systems. To this date, the idealized g-C<sub>3</sub>N<sub>4</sub> structure has not been unambiguously identified in any synthesized samples. As a result, the exact structural characterization of PCNs is still an open question, and no single computational model on its own so far was able to fully explain the measured properties.

Combined theoretical and experimental efforts were able to shed light on some of the structural parameters of PCNs. Gracia *et al.* for example found that corrugation can stabilize heptazine-based PCNs.<sup>26</sup> Li *et al.* found that micro-structural features of PCNs such as H-bonding, interlayer spacing, and stacking configuration are susceptible to temperature variations during synthesis.<sup>27</sup> Salt melts were explored for PCN synthesis and the templating effect from these salts was found to facilitate the synthesis of PCN structures with large cavities, such as poly(triazine imide) (PTI) and poly(heptazine imide) (PHI).<sup>28-30</sup>

Uncertainty with respect to the structure of PCNs is one of several issues that theoreticians face when simulating this new material class. Further complications include the importance of accurately describing the optical properties, which necessitates the use of costly hybrid density functional theory (DFT) methods that augment regular generalized-gradient approximation (GGA) calculations with exact exchange contributions derived from Hartree-Fock wave function theory calculations on the Kohn-Sham orbitals.<sup>31,32</sup> Unfortunately, large system sizes are often required to model PCNs, which can make hybrid DFT calculations computationally unfeasible. Finally, PCNs are characterized by a multitude of intricate structural features such as stacking, edge boundaries, and corrugation which further increases the complexity of model systems.<sup>32-35</sup> The structural complexity of PCNs therefore hampers computational efforts aimed at improving our understanding of their fasci-

nating properties, including strong excitonic effects,<sup>36</sup> charge accumulation,<sup>37–41</sup> and tuning of the optical properties towards more efficient visible light absorption.<sup>16,42</sup>

Most notably, there is significant disagreement in literature between theoretical bandgap predictions and experimentally measured bandgaps. In particular, models for which bandgaps of 3 eV and lower are calculated typically feature a high degree of condensation while elemental analyses of synthesized materials with similar bandgaps show hydrogen contents that are incompatible with the theoretical models.<sup>43–46</sup> The authors are convinced that this discrepancy is the result of the structural complexity of PCNs which is hard to represent properly in simulations.

In this study, we aim at postulating a more complete model system for PCNs. To this end, the relationship between structures and optical properties of PCNs are systemically investigated. Calculations initially focus on exploring individual parameters such as the degree of condensation, increase of dimensionality, and corrugation. To investigate these parameters and to model the polycondensation reaction from monomer to various PCN structures, the thermochemical approach introduced by Botari *et al.*<sup>47</sup> is adopted and extended by incorporating vibrational enthalpy and entropy contributions of the solid-state materials. By varying the chemical potential of  $\text{NH}_3$ ,  $\Delta\mu_{\text{NH}_3}$ , refined thermochemical maps are obtained and reveal a thermodynamic route for the formation of the fully-deaminated PCN structure, typically referred to as  $\text{g-C}_3\text{N}_4$ , via PHI as an intermediate.

The key finding of the present work is that already small domains of  $\text{g-C}_3\text{N}_4$  embedded in less condensed PCN structures are sufficient to obtain bandgaps of 3 eV and lower. Thus, a comprehensive model system is postulated from a combination of the most important structural features explored in this work that affect the stability and optical properties of PCNs. This structure is thermodynamically feasible, shows a bandgap of *ca.* 2.9 eV while retaining a low degree of condensation, and is predicted to form under experimentally accessible conditions. This model constitutes an important step towards a more holistic description of this fascinating material class in atomistic simulations.

## 2 Methodology

### 2.1 Computational Details

All calculations were performed using the Vienna Ab initio Simulation Package (VASP) version of 5.4.4 which employs the projector-augmented wave (PAW) method.<sup>48–52</sup> A plane wave energy cut-off of 400 eV was used and the wavefunction was optimized to an accuracy of  $10^{-6}$  eV. Atomic coordinates were relaxed until forces reached below  $5 \times 10^{-2}$  eV/Å. Gaussian-type finite-temperature smearing was employed with a smearing width of 0.01 eV. Long range interactions were treated with DFT-D3 dispersion correction.<sup>53,54</sup>

The atomic and cell coordinates were relaxed using the exchange-correlation functional by Perdew, Burke, and Ernzerhof (PBE) within the generalized gradient approximation (GGA).<sup>55</sup> Accurate final energy results were then obtained by performing single-point calculations on the PBE-optimized structures using the hybrid functional by Heyd, Scuseria, and Ernzerhof with 25 % exact exchange and a screening factor of  $0.2 \text{ \AA}^{-1}$  (HSE06).<sup>56</sup> The HSE06 functional was found to deliver a good description of the electronic properties of PCNs.<sup>31,32,35</sup>

Atomic coordinates of molecular models were optimized using the ORCA package version 4.21<sup>57,58</sup> using the PBE0 functional,<sup>55,59,60</sup> def2-TZVP basis set, def2/J auxiliary basis set, and DFT-D3 dispersion correction. Then, single point calculations were performed in VASP using the HSE06 functional to obtain final energy results. The pre-optimization in ORCA was found to be necessary because geometry relaxations in VASP regularly did not find the energetic minimum structures for molecules. In particular, corrugation is more pronounced in the ORCA optimized structures, which in fact also give lower total energy results after subsequent HSE06 single-point calculations in VASP. We assume that ORCA, with which we used finite basis sets and a hybrid functional for the relaxation, enabled symmetry breaking more easily compared to the GGA-based VASP plane wave calculations. To avoid spurious interactions between molecules and in case of 2D surface calculations, a vacuum layer of

( $\sim 20 \text{ \AA}$ ) was used and dipole correction was enabled in the relevant directions (molecules: all directions, surfaces: perpendicular to surface). The Monkhorst-Pack scheme was adopted to create  $k$  point grids for Brillouin zone integration.<sup>61</sup> A single,  $\Gamma$ -centered  $k$  point was used for molecular structures. The vibrational contribution was calculated from force constant matrices using the VASP-Phonopy interface.<sup>62-64</sup> A data set of atomic coordinate files of the investigated structures in the VASP-POSCAR file format has been made available.<sup>65</sup>

## 2.2 Thermochemistry

For thermochemical analysis, we consider a simple thermal synthesis which uses melamine as the monomer. The thermochemical stability for each structure is assessed by the formation free energy  $\Delta G_{\text{F}}(T, p)$  using the following equation:

$$\Delta G_{\text{F}}(T, p) = G_{\text{structure}}(T, p) - (n G_{\text{melamine}}(T, p) - m \mu_{\text{NH}_3}(T, p)). \quad (1)$$

Temperature ( $T$ ) and pressure ( $p$ ) are taken into account for the solid-state structures. The free energy of any particular structure under investigation,  $G_{\text{structure}}$ , and of a melamine monomer,  $G_{\text{melamine}}$ , are calculated as follows:

$$G = E^{\text{total}} + F^{\text{vib}} + pV \quad (2)$$

where  $E^{\text{total}}$  is total energy,  $F^{\text{vib}}$  is vibrational free energy. The contribution of vibrational degree of freedom can be obtained from phonon density of states  $\sigma(\omega)$ .

$$\begin{aligned} F^{\text{vib}}(T, \omega) &= \int d\omega F^{\text{vib}}(T, \omega) \sigma(\omega) \\ &= \frac{1}{2} \hbar \omega + k_{\text{B}} T \ln \left[ 1 - \exp \left( \frac{-\hbar \omega}{k_{\text{B}} T} \right) \right] \end{aligned} \quad (3)$$

The gas phase chemical potential of ammonia,  $\mu_{\text{NH}_3}(T, p)$ , which depends on temperature

and partial pressure, is an important term to connect simulations with experimental conditions. We adopt the expression for  $\Delta\mu_{\text{NH}_3}(T, p)$  from Botari *et al.*<sup>47</sup> This expression for the calculated  $\mu_{\text{NH}_3}(T, p)$  is based on the polyatomic ideal gas approximation composed of translational, rotational, vibrational terms:<sup>66-68</sup>

$$\mu(T, p) = E_{\text{NH}_3}^{\text{total}} + E_{\text{NH}_3}^{\text{ZPE}} + \Delta\mu(T, p) + pV \quad (4)$$

$$\begin{aligned} \Delta\mu(T, p) &= \mu_{\text{trans}} + \mu_{\text{rot}} + \mu_{\text{vib}} \\ &= -\frac{1}{2}k_{\text{B}}T \left\{ \ln \left[ \left( \frac{2\pi m}{h^2} \right)^{\frac{3}{2}} \frac{(k_{\text{B}}T)^{\frac{5}{2}}}{p} \right] + \ln \left( \frac{k_{\text{B}}T}{\sigma^{\text{sym}} B_0} \right) - \ln \left[ 1 - \exp \left( -\frac{\hbar\omega}{k_{\text{B}}T} \right) \right] \right\} \end{aligned} \quad (5)$$

where  $k_{\text{B}}$  is the Boltzmann constant,  $m$  is the mass of ammonia,  $\sigma^{\text{sym}}$  is the symmetry number,  $B_0$  is the rotational constant,  $\omega$  is the fundamental modes of the particle,  $\hbar$  is the reduced Planck constant.

To validate our approach, we successfully reproduced published formation free energy trends for PCNs, see Figure S2 and S3.<sup>47</sup> The published trends, however, neglect the influence of vibrational contributions on the free energy of both oligomers and solids. Significant changes can be observed when vibrational contributions are included (see Figure S4).

Finally, the degree of condensation (DoC) is used as a descriptor throughout this work. It is calculated as the percentage quotient between the number of condensation points found in a particular structure and the product of the number of melem units - which are stable intermediates formed from the precursor melamine - that the structure is made up of times the maximum number of condensations that each melem unit in the structure can support (6):

$$\text{DoC} = \frac{\# \text{ of condensations}}{N_{\text{melem}} \times 6} \times 100. \quad (6)$$

### 2.3 Model Systems

In order to simulate the thermodynamics of PCN formation, we simulate the polycondensation thermodynamics from the melamine monomer up to the tetramer phase. The inves-

tigated model systems are illustrated in Figure 1. The investigated 2D- and 3D-periodic

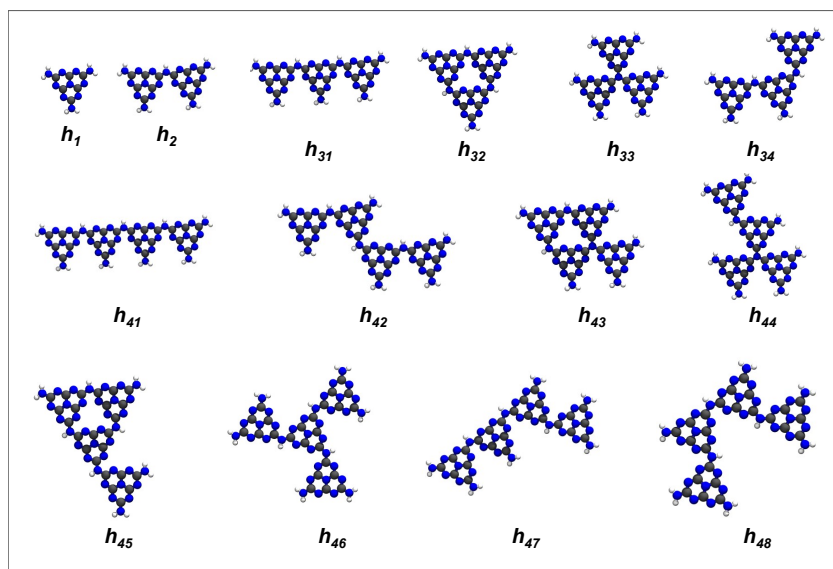


Figure 1: Illustration of molecular oligomer model systems investigated in this study. The models are named after a  $h_{xy}$  naming scheme, where  $x$  is the number of heptazine units and  $y$  is an increasing number that indexes the oligomers.

models are illustrated in Figure 2, while the mixed-motif structures postulated in section 4.5 are shown in Figure S1. The atomic coordinates of all structures were relaxed using the methodology outlined in section 2.1. Even though no constraints or restraints were placed on the models, the melon,  $pg\text{-C}_3\text{N}_4$ , and  $\text{C}_9\text{N}_{13}\text{H}_3$  structures retained an idealized flat configuration, which is known to be a local minimum.<sup>26,34,69</sup> The other periodic structures show various degrees of corrugation. Corrugation is notorious due to the large number of local minima in the coordinate space. While this limitation affects our ability to predict absolute stability values with high confidence, it is only of minor importance when looking at larger scale stability trends, which is the focus of the present work.



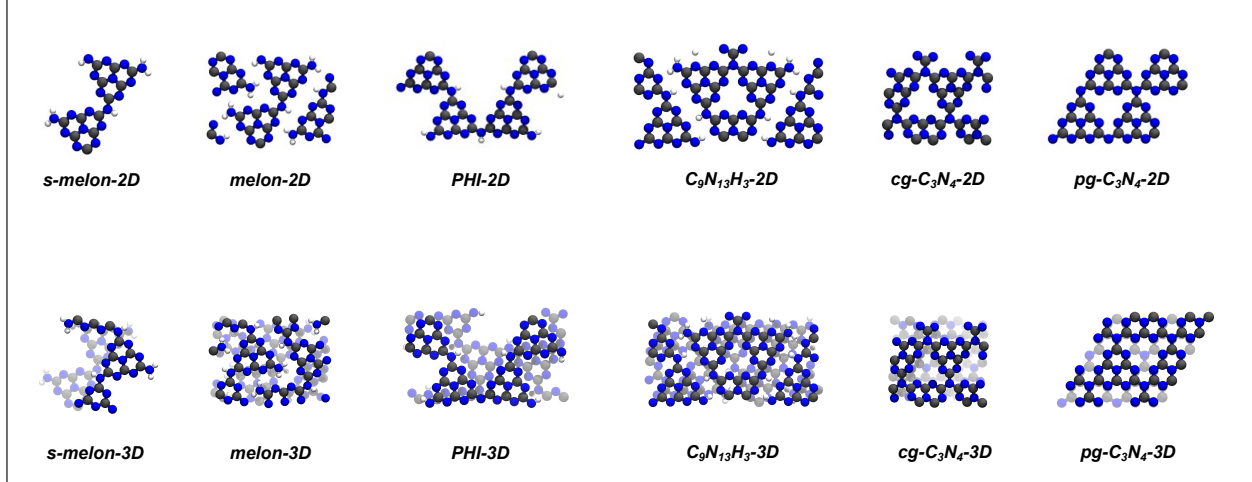


Figure 2: Illustration of periodic 2D surface and 3D crystal models investigated in this study. Structures are composed of s-melon, melon, PHI,  $C_9N_{13}H_3$ , cg- $C_3N_4$ (corrugated), and pg- $C_3N_4$ (planar) structural motifs.

### 3 Results

#### 3.1 Formation Energy Trends for 1D Materials

To understand the condensation process, formation free energy ( $\Delta G_F$ ) phase diagrams are constructed using the melamine monomer and  $NH_3$  molecules as reference. Since there is only one possible configuration to form a dimer, different trimer and tetramer configurations are explored first. All calculated molecular structures are illustrated in Figure 1. The relative stability trends for the trimer and tetramer phases are shown in Figure 3(a) and 3(b), respectively. The phase diagram reveals that two competing condensation processes exist during the molecular oligomerization stage: non-cyclic and cyclic condensation. Non-cyclic condensation is the dominant process at more positive values of  $\Delta\mu_{NH_3}$  while cyclic condensation is the dominant process at more positive values of  $\Delta\mu_{NH_3}$  while cyclic condensation is dominant below  $\Delta\mu_{NH_3}$  values of *ca.* -1.0 eV, both in case of trimers and tetramers.

In case of the tetramer structures, the cyclic  $h_{45}$  and the  $h_{43}$  configurations (see Figure 1) are found to be similarly favorable. Both of these structures contain a condensed ring of three heptazine units ( $h_{32}$ ) with an additional dangling heptazine unit, which is either attached at

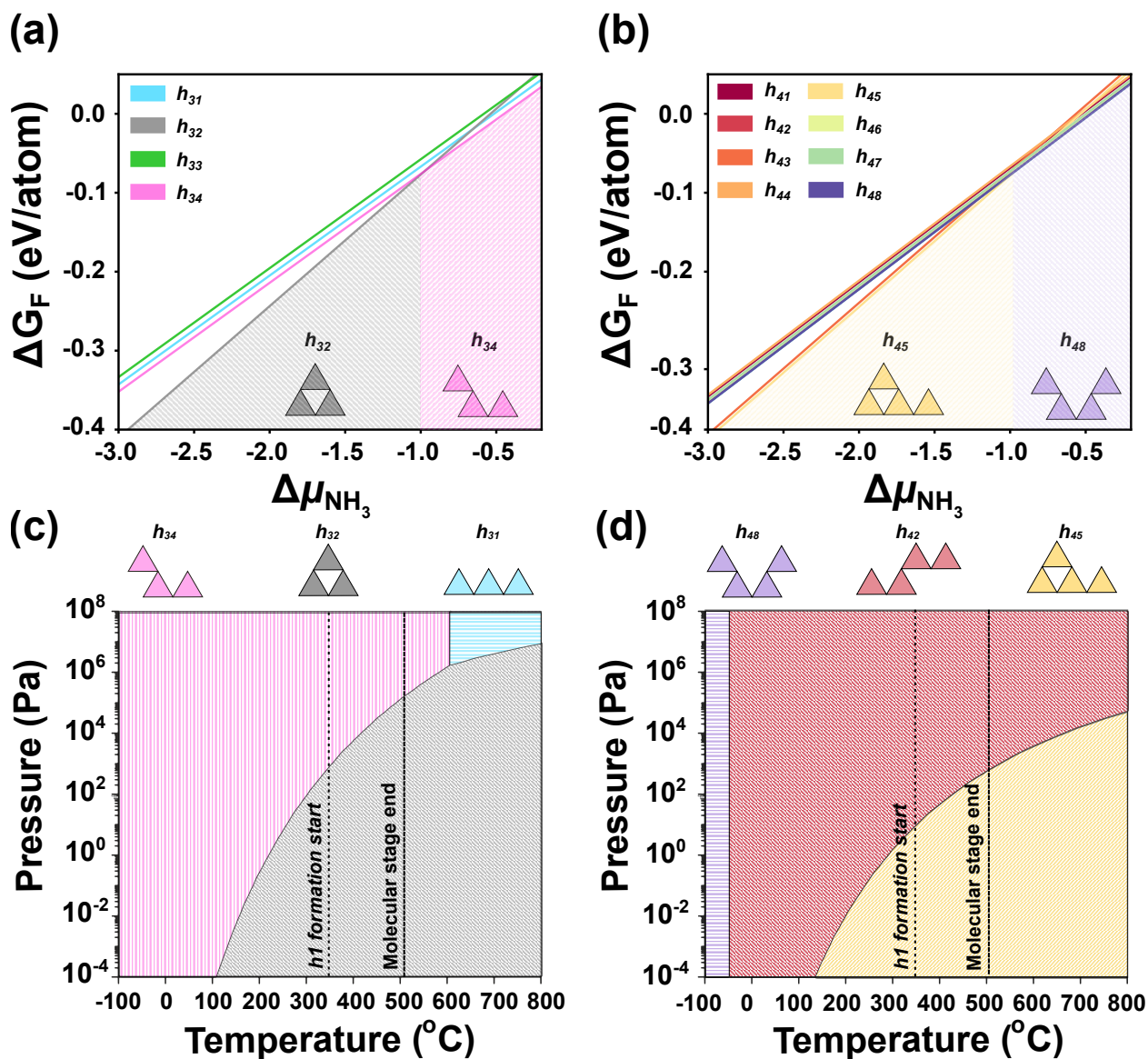


Figure 3: The free energy of formation for all (a) trimer and (b) tetramer structures are shown as function of  $\Delta\mu_{\text{NH}_3}$ . The free energy of formation is normalized to eV/atom to be able to compare structures with different total number of atoms. Free energy results are then expanded into  $T$ - $p_{\text{NH}_3}$ -dependent phase diagrams for the most stable (c) trimer and (d) tetramer structures, respectively. The experimental temperature range for synthesis of these molecular structures is given between the dotted and the dashed line.<sup>21,22,27,70,71</sup>

a terminal ( $-\text{NHR}$ , where  $R = \text{heptazine, h}_{45}$ ) or at a bridging group ( $-\text{NR}$ ,  $\text{h}_{43}$ ). On the other hand, among the non-cyclic configurations,  $\text{h}_{42}$  and  $\text{h}_{48}$  compete as the most stable configurations with only small deviations of  $\Delta G_{\text{F}}$  of  $10^{-4} - 10^{-3}$  eV/atom. These structures as well as  $\text{h}_{41}$  and  $\text{h}_{42}$  actually constitute rotamers which can be converted into each other by rotation around bridging  $R-\text{NH}-R$  moieties. Structure  $\text{h}_{48}$  appears to be slightly more stable at  $\Delta\mu_{\text{NH}_3}$  values close to zero, likely due to stabilizing van-der-Waals interactions that result from this configuration. Both of the angled structures ( $\text{h}_{42}$  and  $\text{h}_{48}$ ) are more stable than the linear structure  $\text{h}_{41}$ . However, the energy differences are small enough that a mixture of all of the discussed configurations may be formed from a thermodynamic point of view.

The  $\Delta G_{\text{F}}$  differences between the most stable trimer and tetramer structures can be illustrated in a more practically-oriented way by expanding  $\mu_{\text{NH}_3}$  into  $T$ - $p$  phase diagrams, see Figures 3(c) and (d). At reported synthetic conditions,<sup>21,22,71</sup> the formation of melem ( $\text{h}_1$ ) begins at *ca.* 350–370 °C (Figure 3 (c) and (d)). From gravimetric analysis it is commonly assumed that formation of molecular oligomer structures is the dominant process until a temperature of *ca.* 500 °C.<sup>70</sup> At higher temperature, more condensed structures (*i.e.*, 2D-condensed polymers) are expected to form. From this analysis, it can be inferred that the more condensed structures  $\text{h}_{32}$  (trimer) and  $\text{h}_{45}$  (tetramer) are most likely to form in the typical experimental temperature regime (500–630 °C)<sup>14</sup> and low  $\text{NH}_3$  partial pressure ( $p_{\text{NH}_3}$ ), whereas the non-cyclic  $\text{h}_{34}$  and  $\text{h}_{42}$  structures are thermodynamically preferred at higher  $p_{\text{NH}_3}$ .

### 3.2 Formation Energy Trends for 2D and 3D Materials

The formation free energy trends for 2D and 3D structures are shown in Figure 4. The melon-2D structure accounts for the most stable structure up to  $\Delta\mu_{\text{NH}_3} = -1.49$  eV. The PHI-2D structure appears as an intermediary phase between  $\Delta\mu_{\text{NH}_3} = -1.49$  and  $-1.68$  eV. For more negative  $\Delta\mu_{\text{NH}_3}$ , the highly-condensed cg- $\text{C}_3\text{N}_4$ -2D structure becomes the most stable phase.

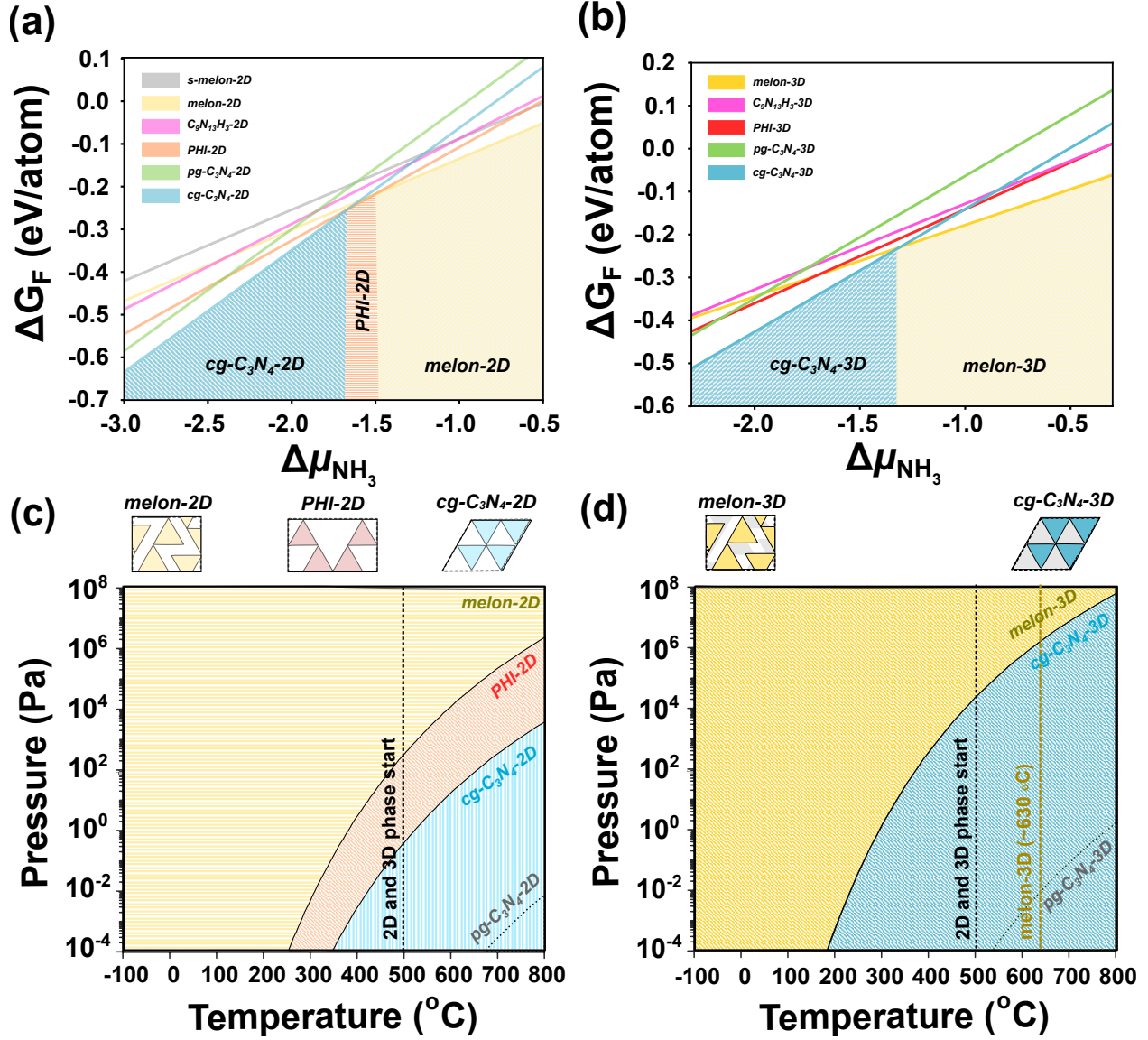


Figure 4: The free energy of formation for all (a) 2D and (b) 3D structures is shown as a function of  $\Delta\mu_{\text{NH}_3}$ . The free energy of formation is normalized to eV/atom to be able to compare structures with different total number of atoms. Then, free energy results are expanded into a  $T$ - $p_{\text{NH}_3}$ -dependent phase diagrams for the most stable (c) 2D and (d) 3D structures, respectively. The experimentally measured temperature range for the formation and the decomposition of PCNs are given as dotted black and yellow lines.<sup>27,70</sup> The dotted grey line indicates the stability region for the fully flat pg- $\text{C}_3\text{N}_4$ -2D/-3D phases which constitutes a local minimum structure and lays behind the more stable corrugated cg- $\text{C}_3\text{N}_4$ -2D/-3D structure.

By deconvoluting  $\Delta\mu_{\text{NH}_3}$  into a  $T$ - $p$  diagram, Figure 4 (c), a similar trend regarding the  $p_{\text{NH}_3}$  is obtained as for the molecular phases, *i.e.*, higher degree of condensation (DoC) can be achieved by reducing  $p_{\text{NH}_3}$  at the experimental temperature conditions (500–630 °C).<sup>14</sup>

In the 3D phase, cg-C<sub>3</sub>N<sub>4</sub>-3D is the most stable structure at  $\Delta\mu_{\text{NH}_3} \leq -1.33$  eV. At more positive values of  $\Delta\mu_{\text{NH}_3}$ , the melon-3D structure becomes more stable. The  $T$ - $p$  phase diagram (Figure 4 (d)) reveals that there is thermodynamic competition between the formation of the cg-C<sub>3</sub>N<sub>4</sub>-3D and melon-3D structures - or, in fact, their coexistence - in the experimental temperature range (500–630 °C) and at a  $p_{\text{NH}_3}$  of 1 atm. This phase border shows that lowering  $p_{\text{NH}_3}$  will make the more condensed cg-C<sub>3</sub>N<sub>4</sub>-3D structure thermodynamically more favourable.

### 3.3 Optical Property Trends

Calculated trends of the HOMO-LUMO gaps for the molecular structures as well as bandgap trends for the periodic structures are listed in Table S1. Figure 5 summarizes the calculated values. Note that HOMO-LUMO gaps for the molecular models are given as average values over all dimers, trimers, and tetramers, respectively.

The optical property results give rise to several noteworthy trends: first, the optical gap decreases as the DoC increases. This trend is particularly apparent for the 2D periodic models. For instance, the melon-2D model, which shows a DoC of 50%, has a *ca.* 0.7 eV larger bandgap than the highly-condensed cg-C<sub>3</sub>N<sub>4</sub>-2D model (DoC = 100%).

Second, as the dimensionality of the system increases from 1D molecules to 2D sheet models to 3D crystal models, the optical gap decreases. This trend is noteworthy in particular for the 2D to 3D transition where the growth mechanism is stacking of the 2D layers, *i.e.* no additional covalent bonds are formed.

Third, corrugation of the structures increases the optical gap slightly. For example, the completely-flat pg-C<sub>3</sub>N<sub>4</sub>-2D model, which constitutes a local minimum configuration of the system, has a *ca.* 0.2 eV smaller bandgap than the corrugated and thermodynamically

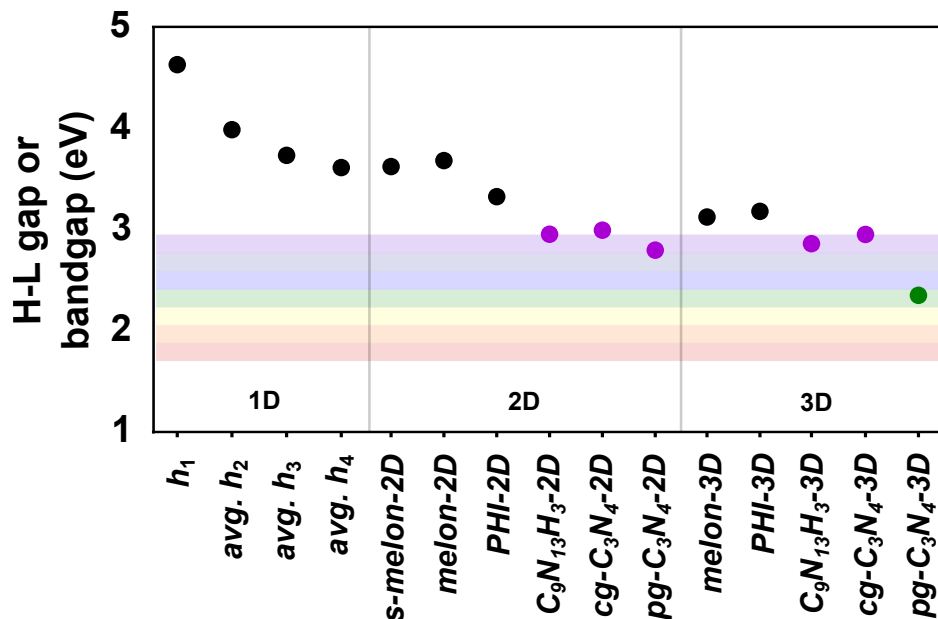


Figure 5: Summary of the calculated optical gap trends; HOMO-LUMO gaps are given for molecules and bandgaps are given for the periodic structures. For simplicity, the averaged HOMO-LUMO gaps are presented for the dimer up to tetramer structures. A color palate is given for reference to roughly indicate the energy range corresponding to visible light.

more stable ( $\Delta E = 0.7$  eV/heptazine unit) cg- $C_3N_4$ -2D system. This effect is even more pronounced for the 3D crystal models, where the non-corrugated system has a narrower bandgap of *ca.* 0.6 eV. At the same time, the interlayer spacing of the non-corrugated model decreases by *ca.* 0.17 Å compared to the corrugated model, indicating significantly stronger interaction between layers.

Lastly, we studied the bandgap as function of an increasing number of heptazine units for hydrogen-terminated nanoribbons. The studied model systems, bandgap results, and a comparison to the optical properties of some key structures investigated above are given in Figure 6. Calculations show that bandgaps converge to a value close to that of the 100 % DoC pg- $C_3N_4$ -2D model for ribbons that are 5–7 heptazine units wide. Already at a width of 3 heptazine units, a significant reduction of the bandgap from *ca.* 3.6 to 3.0 eV is observed. This result suggests that already small areas of g- $C_3N_4$  are sufficient to produce the bandgaps observed for the fully-condensed 2D materials.

Note that corrugation is not taken into account in this test set and thus, values are

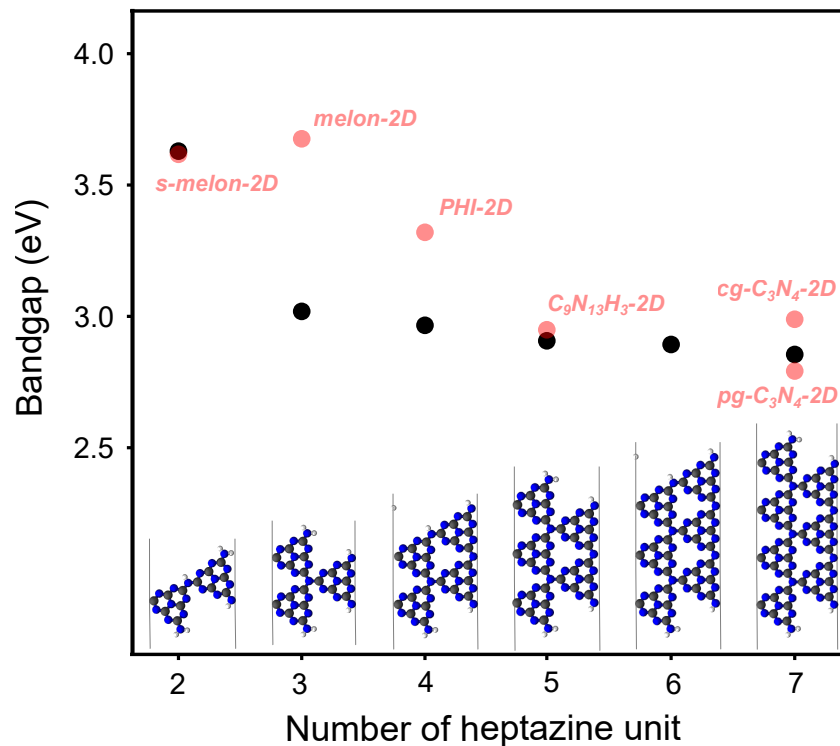


Figure 6: Calculated bandgap trends as a function of the number of heptazine monomers in hydrogen-terminated ribbon models of increasing width. Band gaps of key 2D structures are given in light red for reference (see Figure 5). The ribbon models neglect the influence of corrugation, see text for more details. As the number of heptazine units increases from 2 to 7, the bandgap decreases from 3.6 eV to 2.9 eV, with the most significant decrease observed already from 2 to 3 heptazine units (*ca.* 0.6 eV).

closer to the flat pg-C<sub>3</sub>N<sub>4</sub>-2D model rather than the corrugated cg-C<sub>3</sub>N<sub>4</sub>-2D model. For larger ribbons (5–7 units), it is expected that bandgap values would shift to larger values if corrugation was accounted for, analogous to the difference between cg- and pg-C<sub>3</sub>N<sub>4</sub>-2D.

### 3.4 The Influence of Hydrogen Bonding on the melon Structure

The melon-2D and melon-3D models are set apart from the other structures because their individual strings interact via hydrogen bonds exclusively rather than via any bridging covalent bonds. The investigated melon structures exhibit high thermodynamic stability both in the literature<sup>35,47</sup> and our calculations, as shown in Figure 4. However, the formation energy trends were obtained by optimizing the atomic configurations at a temperature of 0 K; any temperature dependence of the calculated Gibbs free energy values is accounted for using the approximations described in the method section. Notably, it is known from atomistic and experimental studies on the structure of water that hydrogen bond lengths elongate quadratically as a function of increasing temperature.<sup>72</sup> The calculations presented here therefore likely underestimate the separation distance between the hydrogen-bonded melon strings and overestimate their stability at ambient temperature and particularly at elevated temperature during synthesis.

To account for this shortcoming, another melon-based periodic model is investigated: the single-stringed model, s-melon-2D, as presented in Figure 2. This structure constitutes an extreme case, *i.e.* where melon strings are separated far enough that no more interaction via hydrogen bonds takes place between them. This model is therefore likely more representative for the string separation distance at high temperatures, such as during synthesis. Figure 7 compares the  $T$ - $p$ -dependent stability of the favourable PHI and cg-C<sub>3</sub>N<sub>4</sub> structures with the s-melon structure instead of the hydrogen-bonded melon-2D structure shown in Figure 4.

By comparing Figure 7 and Figure 4, it becomes clear that hydrogen bonding significantly contributes to the stability of the melon models. The exclusion of this contribution shifts the



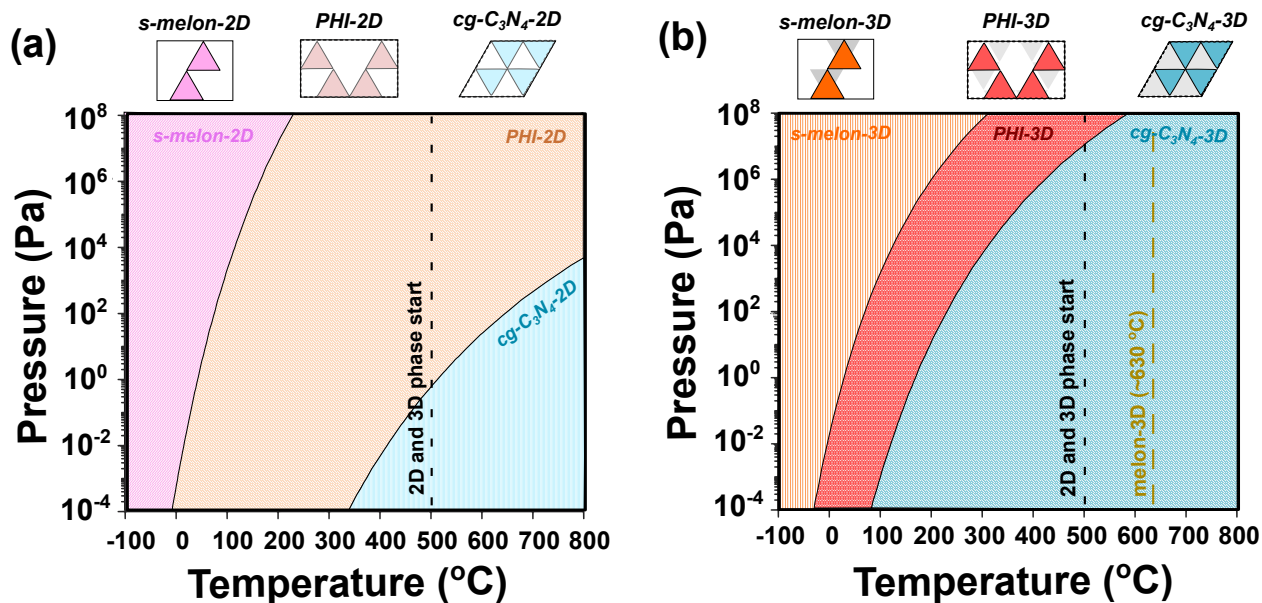


Figure 7: Formation free energy phase diagrams of 2D and 3D structures updated from Figure 4. The hydrogen-bonding stabilized melon-2D/-3D structures are excluded, instead the single-string *s-melon-2D*/*-3D* structures are shown. The dotted and the dashed line indicated the experimentally observed temperature where formation of 2D and 3D structures begins<sup>18,27,70</sup> and where the melon-3D structure was found to form,<sup>14</sup> respectively.

stability region of *s-melon-2D* structure in Figure 7 a) to a lower temperature and the *PHI-2D* structure now appears to be the most favourable configuration at reported experimental synthetic conditions as indicated by the dotted line.<sup>18,27,70</sup> In case of the 3D models, Figure 7 (b) shows that now, the *cg-C<sub>3</sub>N<sub>4</sub>-3D* and *PHI-3D* structural motifs are in thermodynamic competition, which means that a mixture of both structure can be expected to form under typical synthetic temperature conditions (500–630  $^{\circ}\text{C}$ ).

## 4 Discussion

The purpose of this study is to elucidate the relationship between the structure of PCN materials and the corresponding optical properties from a thermodynamic point of view and as a function of material dimensionality. In the following, three key structural parameters that greatly affect the optical properties will be discussed in more detail based on the presented calculation results: (i) degree of condensation, (ii) stacking, and (iii) corrugation.

### 4.1 Correlation between Degree of Condensation and Synthetic Conditions

This section discusses in detail how different synthetic conditions can facilitate different degrees of condensation (DoC) of the synthesized material, according to the calculated formation energy trends. Figure 8 summarizes the formation free energy trends for the most stable structures presented in Figures 3, 4, and 7. An unfiltered overview containing all structures is shown in Figure S5. In this depiction, emphasis is placed on highlighting the change of trends of the thermodynamically preferred structure as a function of  $\Delta\mu_{\text{NH}_3}$ , *i.e.* at various  $T$  and  $p$  conditions.

The formation free energy,  $\Delta G_{\text{F}}$ , is calculated for each structure from  $\text{NH}_3$  and melamine as the educts. The middle-ranged cyan, black, yellow, blue, and orange lines represent the  $T$ - $p$  parameter space that can be achieved under typical laboratory conditions.

From the formation energy trends, it is evident that the DoC is proportional to  $\Delta\mu_{\text{NH}_3}$ ; structures with a higher DoC become more favourable as  $\Delta\mu_{\text{NH}_3}$  becomes more negative. In the aforementioned middle range (blue to cyan lines), all structure show similar thermodynamic stability. We can therefore conclude that from a thermodynamic perspective, the experimentally synthesized material most probably is a mixture of these different structural motifs with no strong preference for any one particular motif.

In addition, the results suggest that certain structural motifs may become dominant

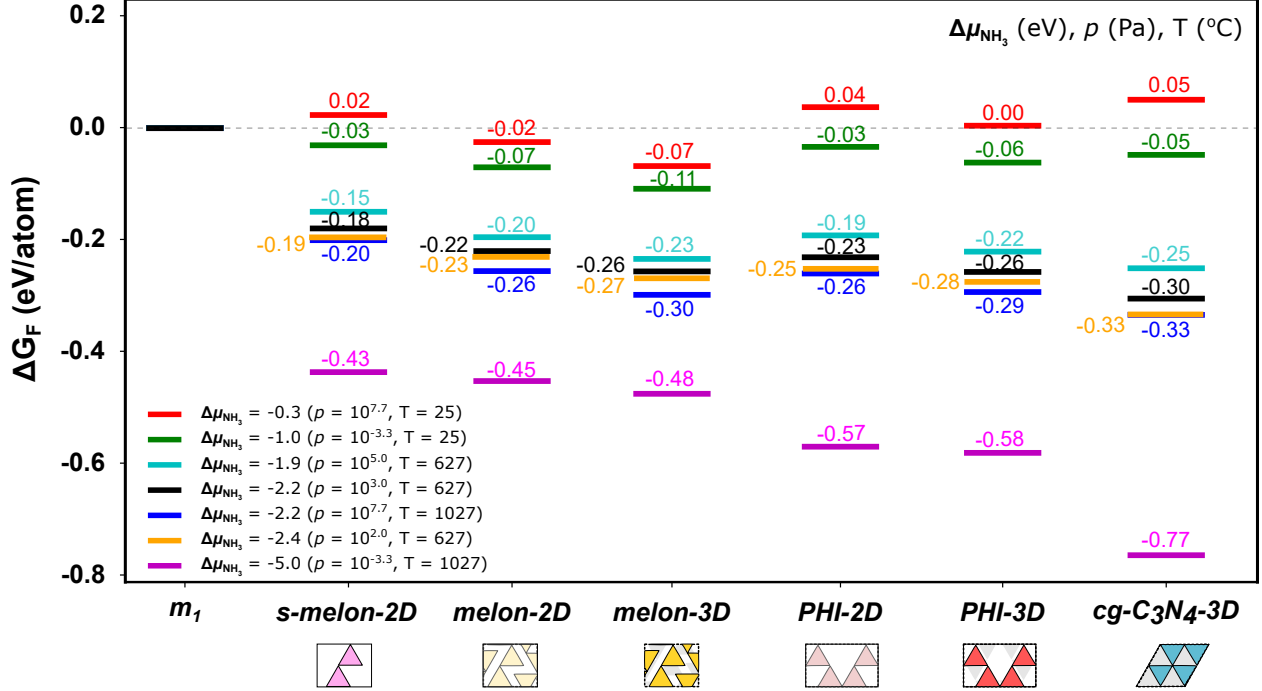


Figure 8: Free energy of formation for key 2D and 3D structures as a function of a selected set of  $\mu_{\text{NH}_3}$  conditions. The free energy of formation is normalized to eV/atom to be able to compare structures with different total number of atoms.

when specific synthetic conditions are enforced. On one extreme end of the  $T$ - $p$  spectrum, we predict that the less-condensed melon string structures can be enforced by performing the synthesis at low temperature conditions and high  $p_{\text{NH}_3}$ , for example in a closed reaction vessel (red and green lines). On the other extreme end, if the synthesis is performed at high temperature and low  $p_{\text{NH}_3}$ , for example in a reaction vessel with an applied vacuum (magenta line), the more condensed cg-C<sub>3</sub>N<sub>4</sub> and PHI structures become favourable. While these extreme cases are not representative of conditions that can be readily achieved in the laboratory, they serve to illustrate the influence of the parameters of temperature and pressure on the expected composition of the PCN material.

Therefore, in order to obtain a PCN with a high DoC and a optical gap of 3 eV or less, these computational trends suggest that high temperature and low  $p_{\text{NH}_3}$  conditions should be maintained during the synthesis. These calculated trends are corroborated by experiments by Inoki *et al.*,<sup>73</sup> who reported successful synthesis of a g-C<sub>3</sub>N<sub>4</sub> structure under controlled

low  $p_{\text{NH}_3}$  (*ca.*  $9.0 \times 10^3$  Pa) at 550 °C. Their synthesized material shows a bandgap of 2.03 eV with an average crystal size of less than 3 nm. On the other hand, Lotsch *et al.* showed that formation of the melon structural motif can be promoted by conducting synthesis in a closed ampule at 630 °C.<sup>14</sup> Further condensation of the melon strings is likely hindered by the relatively high  $\text{NH}_3$   $p_{\text{NH}_3}$  within the ampule. Both of these experimental observations are in good agreement with the predicted trends presented in this work (Figure 4(d)).

Finally, the presented results may help to reconcile conflicting observations from theory and experiments. While published theoretical results predict that high DoC is a requirement to achieve the desired bandgap, experiments measure bandgaps of 2.6–2.7 eV for materials where elemental analysis shows high H content that would indicate a low DoC.<sup>18,22,74</sup> According to the presented trends, the synthesized material likely contains a mixture of different more or less condensed structural motifs, giving rise to desirable optical properties in  $\text{g-C}_3\text{N}_4$ -like domains embedded in a matrix of less-condensed PCN such as the melon string motif. Consequently, this conclusion raises a follow-up question: how large do these highly-condensed domains need to be in order to exhibit the desired properties? This question will be addressed in section 4.3.

## 4.2 Interconversion

It is clear from the presented computational trends that there is thermodynamic competition between the melon-3D structure and the idealized, fully-condensed  $\text{cg-C}_3\text{N}_4$ -3D structure for the end product. Consequently, the question arises if and how interconversion can take place between these structure. More specifically, in this section we discuss whether a thermodynamic pathway exists to convert these phases into each other, for example by annealing the synthesis product under specific conditions.

From a structural point of view, direct conversion from melon to the fully-condensed structure is not straightforward (DoC = 50% for melon, DoC = 100% for  $\text{cg-C}_3\text{N}_4$ ). It is therefore reasonable to assume that the PHI structure (DoC = 75%) may be an interme-

diate structure connecting them. In fact, the PHI structure has already been successfully synthesized, indicating that this structure is at least metastable, if not thermodynamically favourable under specific conditions.<sup>75–80</sup> We therefore hypothesize that the large pores in the PHI structure may be filled with heptazine monomers under certain conditions to give the  $cg-C_3N_4$  structure. Selected hypothetical pathways and their associated reaction free energy trends at different  $T$ - $p$  conditions are summarized in Figure 9. More detailed  $p$ - $T$

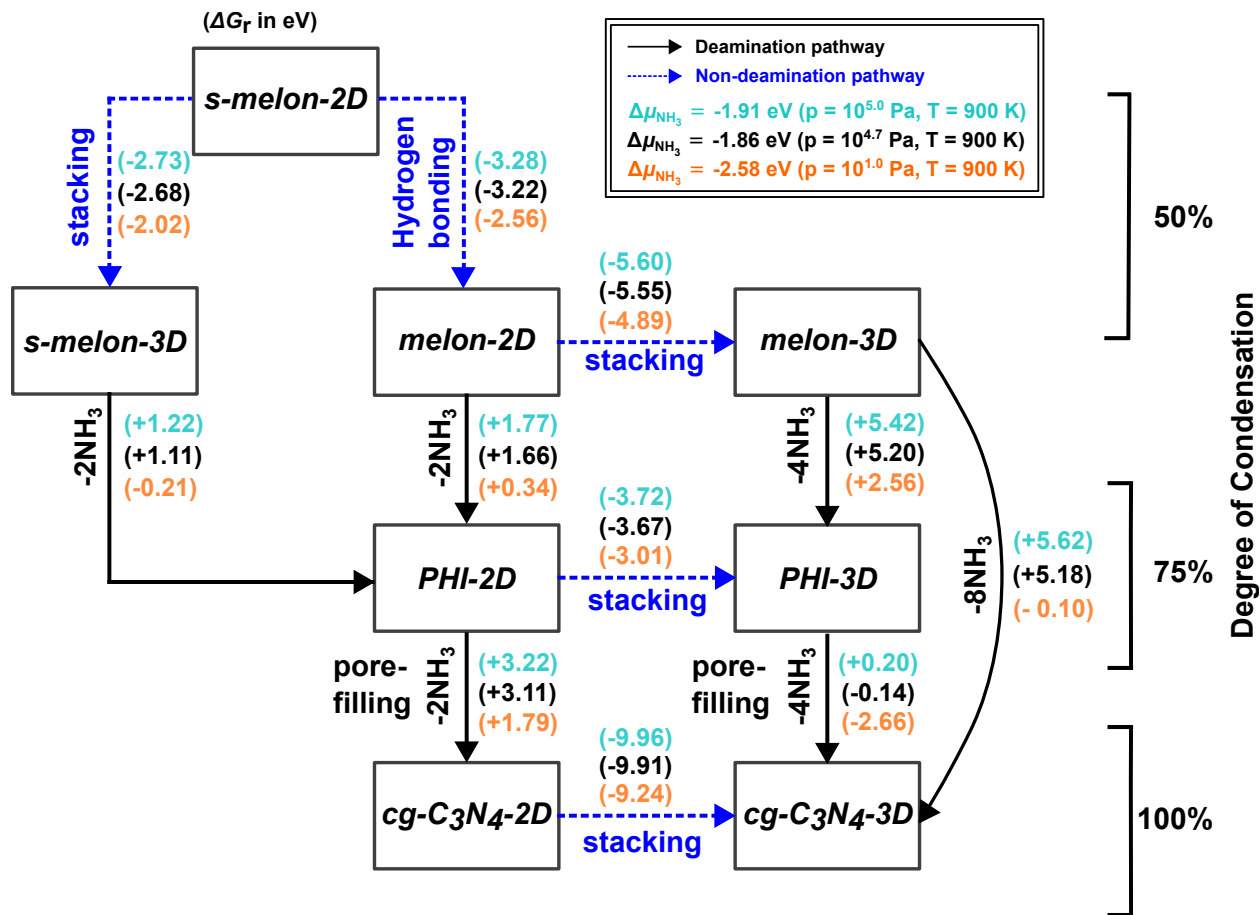


Figure 9: Reaction flow chart connecting structures via the calculated reaction free energy,  $\Delta G_r$ , which depends on  $\Delta\mu_{NH_3}$  ( $-2.6$  eV  $<$   $\Delta\mu_{NH_3}$   $<$   $-1.9$  eV). Temperature is fixed to 628 °C, which constitutes the maximum temperature before carbonization of the material sets in, so that the reaction free energy trends depend solely on  $p_{NH_3}$ . Two reaction mechanisms are suggested: i) The non-deamination pathway involving stacking and hydrogen bonding and ii) the deamination pathway involving release of  $NH_3$ . The structures are classified by their degree of condensation (DoC). The "pore-filling" route is suggested to connect PHI structure to  $cg-C_3N_4$  structure; see text for more details.

phase diagrams from which these trends were summarized are shown in Figure S6.

Here, the reaction free energy  $\Delta G_r$  between any product and an educt state is calculated as

$$\Delta G_r(T, p) = n G^{\text{product}}(T, p) - m G^{\text{educt}}(T, p) - o G^{\text{NH}_3}, \quad (7)$$

where  $G^{\text{product}}(T, p)$ ,  $G^{\text{educt}}(T, p)$ , and  $G^{\text{NH}_3}(T, p)$  constitute the Gibbs free energy of the product and educt configurations as well as the  $\text{NH}_3$  molecule, respectively, and  $n$ ,  $m$ , and  $o$  are stoichiometric factors.

The trends shown in Figure 9 were calculated at 628 °C, which is close to the decomposition temperature of *ca.* 630 °C.<sup>70</sup> The reaction profile can then be controlled by  $p_{\text{NH}_3}$ . The proposed reaction profile conveys two important thermodynamic factors that determine the end structure at the respective conditions:

1. The non-deamination pathway is thermodynamically more favourable than the deamination pathway because stabilization occurs via hydrogen bonds and/or stacking. However, this process does not increase the DoC.
2.  $p_{\text{NH}_3}$  plays a pivotal role in controlling the reaction free energy of the deamination pathways, which increases the DoC.

From these trends, it is clear that the melon structure represents a thermodynamic sink. The conversion from melon-3D to the idealized  $\text{cg-C}_3\text{N}_4$ -3D structure only becomes exothermic at drastic conditions of  $p_{\text{NH}_3} = 10$  Pa. The same is true for the deamination pathway leading from s-melon-3D to PHI-2D. However, if the PHI-2D stage can be reached, which will likely be in equilibrium with the melon-2D structure due to similar formation free energy trends from s-melon-2D, the subsequent stacking to PHI-3D and pore filling reaction to  $\text{cg-C}_3\text{N}_4$ -3D, which already becomes spontaneous close to atmospheric pressure, are significantly downhill.

To develop a conversion strategy, it is crucial to determine from which point in this flowchart one starts. For example, if synthesis of a PHI material has already succeeded, for

example with the help of templating effects,<sup>77,78</sup> further condensation due to pore filling is possible at comparatively mild conditions. However, converting a melon-3D material into cg-C<sub>3</sub>N<sub>4</sub>-3D may require drastic conditions. When synthesis starts from the educts, a mixture of melon-3D and more condensed material, as signified by the idealized cg-C<sub>3</sub>N<sub>4</sub>-3D system, can be expected due to thermodynamic competition of the s-melon-2D → s-melon-3D and the s-melon-2D → melon-2D pathway.

### 4.3 Influence of Stacking *vs.* Lateral Condensation

The presented results show that stacking, *i.e.* the 2D → 3D transition, is thermodynamically more favorable than condensation or pore filling reactions. Furthermore, a central conclusion of sections 4.1 and 4.2 is that the synthesized material is most likely a mixture of structures, particularly of the melon-3D structure and partially pore-filled PHI-3D. As mentioned at the end of section 4.1, we now face an important question: how big do these highly-condensed domains, which are likely interspersed throughout a host matrix of less strongly condensed melon- or PHI-type structures, need to be in order for the material to exhibit the bandgaps commonly measured in experiments?

In order to investigate this question, we performed a convergence study for strongly condensed carbon nitride nanoribbons of increasing width, see Figure 6. Results show that the optical gap of a ribbon structure composed of 7 or more heptazine units ( $E_{\text{gap}} = 2.85$  eV) has reached that of the fully-condensed structures (cg-C<sub>3</sub>N<sub>4</sub>-2D: 2.99 eV, pg-C<sub>3</sub>N<sub>4</sub>-2D: 2.79 eV). This result underlines that small domains of strongly-condensed PCN of *ca.* 3–4 nm<sup>2</sup> can already exhibit the desired optical properties. Even though our computational predictions show that the material prefers to grow via stacking rather than laterally, condensation of only 7 heptazine units should be readily possible. This extrapolated minimum crystalline size is in good agreement with experiments by Inoki *et al.*, who calculated a bandgap of 2.06 eV for PCN crystals of *ca.* 3 nm size.<sup>73</sup>

Furthermore, the average HOMO-LUMO gap of all studied tetramers was computed to

be 3.61 eV, which is comparable to that of the melon 2D structures (3.62 eV and 3.68 for s-melon-2D and melon-2D, respectively; see Table S1). While the absolute values of molecular HOMO-LUMO gaps and bandgaps from periodic calculations are not directly comparable, this trend is still noteworthy. It is also corroborated by a combined experimental–theoretical study by Li *et al.*, who report that the optical gap of heptazine oligomers rapidly converges with size.<sup>27</sup> Therefore, this result not only emphasizes again that a high DoC is a key driving force for red shifting of the optical gap, but is also in a good agreement with the ribbon model convergence study which shows that only small domains of high condensation PCNs are required to produce a desirable bandgap.

#### 4.4 Influence of Corrugation

Corrugation of carbon nitride materials is a significant factor in terms of thermodynamic stability and optical properties. Using GGA-DFT and MP2 methods, Gracia and Kroll found that corrugation enhances the thermodynamic stability of condensed carbon nitride structures by relieving the repulsive interaction between adjacent lone-pair electrons of the nitrogen atoms.<sup>26</sup> This conclusion is in agreement with many other published studies<sup>26,34,69,81</sup> as well as the simulation results presented here. For example, our calculations show that the corrugated fully-condensed cg-C<sub>3</sub>N<sub>4</sub>-2D model is more stable than its fully flat counterpart pg-C<sub>3</sub>N<sub>4</sub>-2D ( $\Delta E = 0.7$  eV/heptazine unit). In terms of optical properties, corrugation increases the bandgap, see Table S1. For example, the flattened pg-C<sub>3</sub>N<sub>4</sub>-3D structure has a 0.6 eV narrower bandgap compared to the corrugated — and thermodynamically more stable — cg-C<sub>3</sub>N<sub>4</sub>-3D structure.

Out-of-plane corrugation of the material occurs in order to minimize repulsive interactions between adjacent N atoms.<sup>26</sup> Here, structural factors contributing to corrugation are examined in more detail, namely the DoC, lateral crystallite size, and stacking. To this end, we compare the calculated root-mean-square deviations (RMSD) of the out-of-plane shift of atomic coordinates for different 1D, 2D, and 3D structures, see Table S2.



First, lateral crystallite size is examined. The RMSD shift increases from 0.01 Å for the heptazine monomer ( $h_1$ ) up to 0.25 Å for the pentamer ( $h_{51}$ ). This result suggests that larger structures corrugate more easily. Section 4.1 already established that the experimental material is most likely a mixture of different structural motifs and section 4.3 established that already small areas of g- $C_3N_4$  can exhibit bandgaps of 3 eV and less. In light of these trends, the present results suggest that in order to achieve a desirable bandgap, a material with only small connected patches of the same structural motif, thereby avoiding corrugation, is desirable. A recent study by Mitoraj *et al.* has used this principle to good effect.<sup>17</sup> The group employed functionalization with a small fraction of azo-linkers in the inner domain to trigger local flattening of the material, thereby redshifting the absorption spectrum.

The DoC can have an even more profound impact on corrugation compared to crystallite size. For example, comparing RMSD shifts for the melon-2D (0.00 Å), PHI-2D (0.57 Å), and cg- $C_3N_4$ -2D (0.80 Å) structures in Table S2, it becomes apparent that corrugation increases as the DoC increases, which counteracts the trend of narrowing bandgaps with increasing DoC (see Table S1). This result once again emphasizes that if the goal is to obtain a PCN material with low bandgap, connected areas of the same structural motif should be kept small since corrugation becomes more pronounced as these areas increase in size.

Finally, stacking appears to inconsistently affect the RMSD shift of the atomic coordinates. For example, the out-of-plane RMSD shifts of atoms in the 2D and 3D cg- $C_3N_4$  models are close to identical (see Table S2). The bandgaps of these models are close to identical, see Table S1. On the other hand, the bandgap of the fully-flattened pg- $C_3N_4$  model is reduced by 0.44 eV due to stacking. Going from PHI-2D to PHI-3D, the extent of corrugation decreases, thereby slightly reducing the bandgap. This result indicates that at least based on the present data set, there is no obvious systematic trend connecting stacking and corrugation. Therefore, any new model system requires detailed investigation in this regard.

To summarize, corrugation has a profound impact on the stability and electronic struc-

ture of carbon nitride materials. In calculations, corrugation is found to stabilize structures thermodynamically and to increase the bandgap. The latter point is two-pronged: corrugation weakens the  $\pi$ - $\pi$  interactions in the lateral direction but also weakens interlayer interactions perpendicular to the layers. From these results, we hypothesize that if the goal is to achieve a material with a small bandgap, synthetic conditions should be optimized to yield a PCN consisting of small domains of the same structural motif since corrugation becomes more pronounced with increasing domain size. As discussed in section 4.3, small domains of g-C<sub>3</sub>N<sub>4</sub> material interspersed in a host matrix of less-condensed material are sufficient to obtain a desirable bandgap.

## 4.5 Postulation of a More Complete Computational Carbon Nitride Model

In this final section, we aim to combine the insights gained throughout this study to postulate a more complete model for the computational investigation of PCNs. While the experimental material is arguably too complex to be treated with any one separate model, we are convinced that there is nevertheless great value in taking steps towards representing as many of the intricacies of this fascinating material class as possible in simulations.

The new model, herein referred to as the "mixed" model, should satisfy the following conditions:

1. The melon structure (50% DoC) should be represented in the model as it constitutes one of the thermodynamically most stable structures found in the present study.
2. The PHI model (75% DoC) is another thermodynamically stable candidate structure that warrants representation, also because successful synthesis of this motif has been reported using a templating method with salt melts.<sup>28,80,82</sup>
3. From bandgap results in this study, only the fully condensed cg- and pg-C<sub>3</sub>N<sub>4</sub> structures can sufficiently explain the experimental bandgap. The planarized pg-C<sub>3</sub>N<sub>4</sub>-3D struc-

ture gives a bandgap as low as 2.35 eV. Calculated free energy trends suggest that these structures form under low  $p_{\text{NH}_3}$  conditions. This 100% DoC structure should therefore be represented as well.

4. Results on the influence of corrugation as well as the presented lateral size *vs.* bandgap data show that small domains of g-C<sub>3</sub>N<sub>4</sub> with low corrugation are sufficient to achieve a narrower bandgap. The model size, therefore, can remain overall small, with rapid alternations between the above structural motifs.

The resulting model as well as a comparison between its DoC and optical properties with those of its three parent structures is illustrated in Figure 10. Shown here is only the most promising mixed model with 57% DoC. Three other structures with DoC up to 71 % were investigated as well and are shown in the Supporting Information, see Figure S1 for illustrations of their structures and Table S1 for the optical properties.

Because the fully-condensed structural motif (red hexagon) is confined in a small domain, only mild corrugation occurs (0.573 Å *vs.* 0.804 Å for cg-C<sub>3</sub>N<sub>4</sub>) and the resulting optical bandgap is *ca.* 2.9 eV, see Table S1. It is noteworthy that the optical bandgap of the mixed structures is lower than that of cg-C<sub>3</sub>N<sub>4</sub>-3D, likely due to the aforementioned encapsulation and local flattening. This result confirms the initial hypothesis that extended condensed structures are not necessary to achieve a desirable bandgap, and highlights that mixed structures can easily give rise to low bandgaps.

To the best of our knowledge, this is the first time that a model system capturing this many important facets of PCNs at once is presented in literature. This study, however, is limited to the structure of the pure PCN materials and does not take into account functional end groups such as -N-H and -N-CN which may be able to further adjust the local electronic structure.<sup>83</sup> The influence of functional groups on electronic properties and reactivity will be explored in the future using this model system as basis.

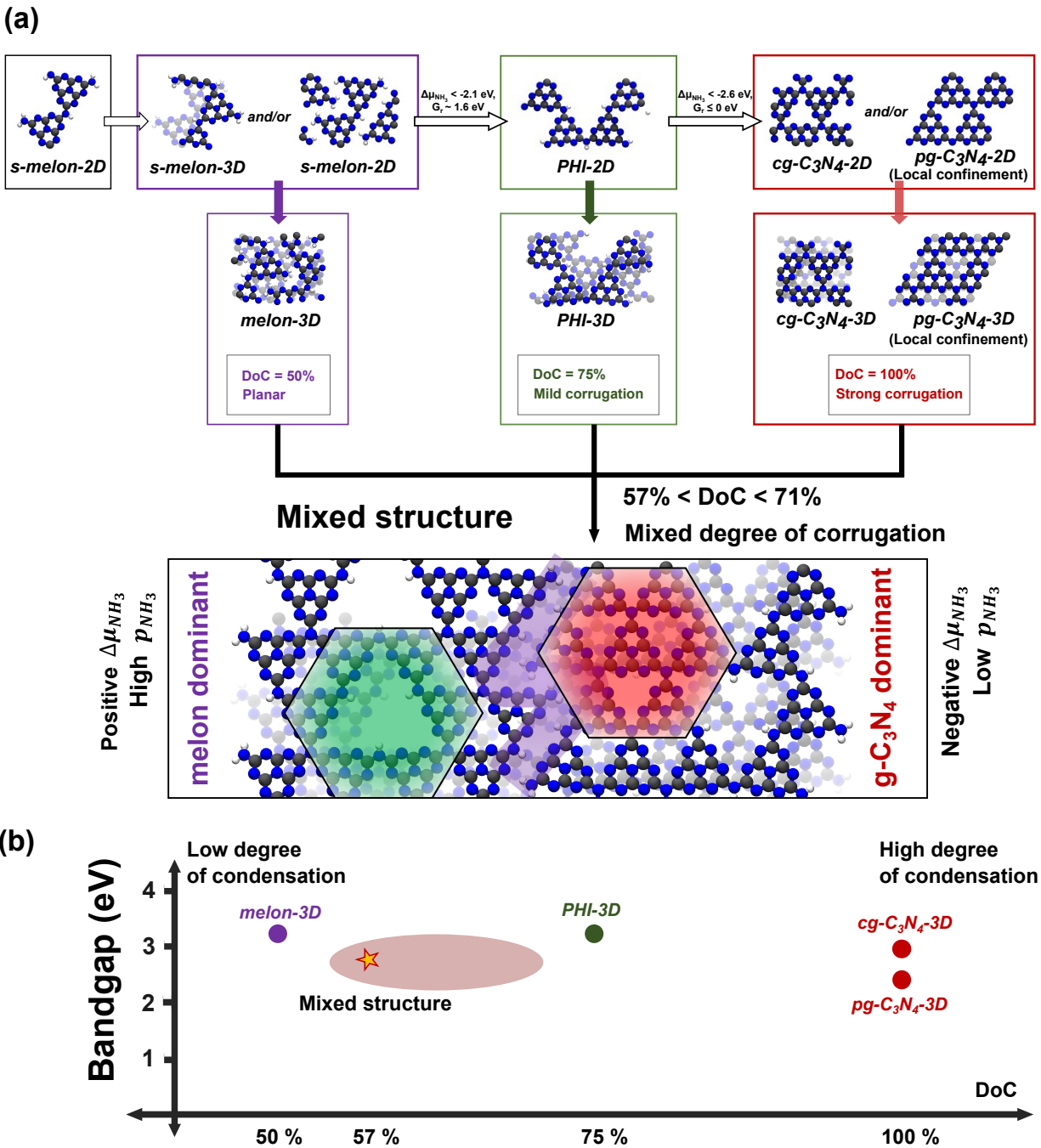


Figure 10: (a) Illustration of the postulated "mixed" PCN model as well as the parent structures it is composed of. (b) Calculated bandgaps for the mixed structural motif as well as for the parent structures as a function of the DoC. The oval shape indicates the range of DoCs and bandgaps obtained for the four tested mixed models; the yellow star indicates the most promising model that is also depicted in (a).

## 5 Conclusion

The thermodynamic stability and the optical properties of heptazine-based carbon nitride materials were investigated using accurate hybrid density functional theory calculations. Three structural parameters were identified that strongly affect the optical properties:

1. degree of condensation (DoC; decreases bandgap and decreases stability),
2. stacking (decreases bandgap and increases stability),
3. and corrugation (increases bandgap and increases stability).

Materials with a high DoC also show pronounced corrugation, which presents a dilemma if material optimization towards narrow bandgaps is the goal. Materials with high DoC and pronounced corrugation form at conditions where the chemical potential of  $\text{NH}_3$ ,  $\mu_{\text{NH}_3}$ , is strongly negative, *i.e.* at high temperature and low  $p_{\text{NH}_3}$ . The melon string structure is preferred at less negative  $\mu_{\text{NH}_3}$  but exhibits a large bandgap. We identified interconversion pathways starting from the melon string structure towards more condensed structures. However, from the relatively small differences in thermochemical stability between these structures, it is expected that materials synthesized under typical experimental conditions consist of a mixture of more and less condensed structural motifs. The thermodynamic preference for stacking over lateral condensation likely further discourages formation of extended areas of the same motif.

From the calculated trends, we postulate a complex computational model that combines features of the melon string, poly(heptazine imide) (PHI), and g- $\text{C}_3\text{N}_4$  model systems. This mixed structure shows a similar thermodynamic stability region as its parent molecules and exhibits, despite its lower DoC of 57%, a narrower bandgap of 2.9 eV compared to the fully condensed but strongly corrugated cg- $\text{C}_3\text{N}_4$ -3D model. The bandgap is likely a result of local flattening of the small, encapsulated, strongly-condensed motif featured in the model.

The present study therefore illustrates that the experimentally well established favorable optical properties of PCNs can emerge from comparatively small g- $\text{C}_3\text{N}_4$  domains embedded

in a framework of thermodynamically more stable and less condensed motifs like the melon string or PHI structures. In future studies, the presented computational model will be used to explore the effects of functionalization and templating ions on the stability, catalytic activity, and optical properties of PCNs.

## Acknowledgement

This work was funded by the Deutsche Forschungsgemeinschaft (DFG — German Research Foundation) through TRR 234 CataLight (project no. 364549901) as well as JA 1972/27-1 (project no. 428764269). Computational resources were provided by the state of Baden-Württemberg through bwHPC and the German Research Foundation (DFG) under Grant No. INST 40/467-1 FUGG. C.I. acknowledges the German Academic Exchange Service (DAAD, Ref. No. 91676720). I.K. acknowledges the support of the Alexander von Humboldt Foundation through the Humboldt Research Fellowship.

## Supporting Information Available

### 6 Supporting information

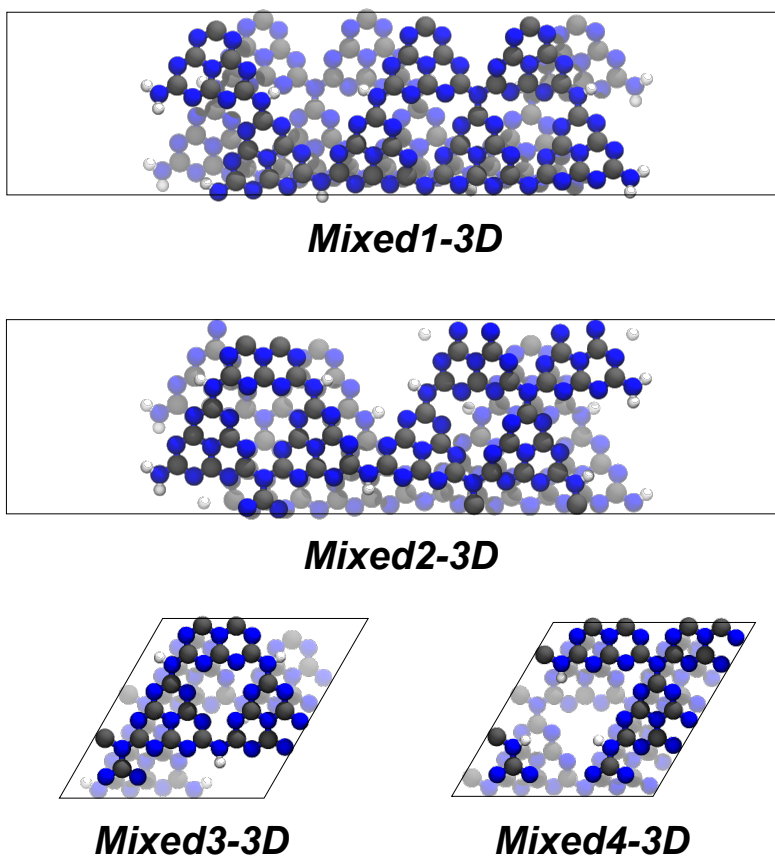


Figure S1: Proposed structures of the mixed motifs used in the study. The structures are composed of the PHI and  $\text{cg-C}_3\text{N}_4$  structure because of their high DoC (79%–94%). The structures of *Mixed1-3D* and *Mixed2-3D* have the edge boundaries which reduce the corrugation. The both *Mixed1-3D* and *Mixed2-3D* are distinct from the sequence of the structural motifs. The *Mixed3-3D* is made of inclusion of PHI structure within  $\text{cg-C}_3\text{N}_4$  domain to both layers and the *Mixed4-3D* is constructed of  $\text{cg-C}_3\text{N}_4$  layer (upper) and PHI layer (bottom), respectively.

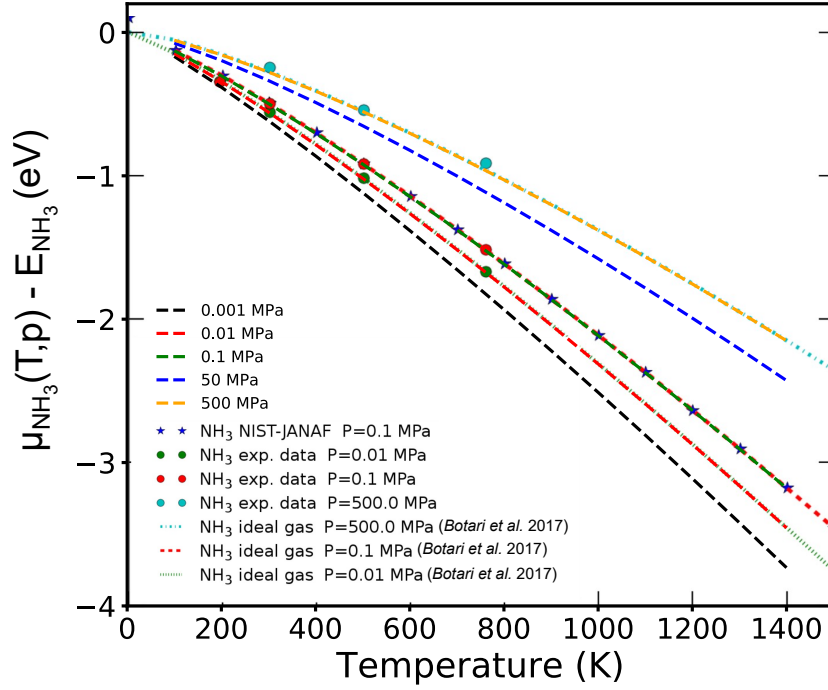


Figure S2: The evaluation of the calculated chemical potential of ammonia used in this study. The reference plots are taken from the NIST-JANAF<sup>84,85</sup> and the literature.<sup>47,86</sup> The dotted points ( $\text{NH}_3$  NIST-JANAF and  $\text{NH}_3$  exp. data) and small dotted lines ( $\text{NH}_3$  ideal gas) are taken from the experimental and the literature, respectively. The bold dashed line illustrates the calculated  $\Delta\mu_{\text{NH}_3}(T, p)$  in this study. Then we added two  $p_{\text{NH}_3}$  conditions of 0.001 MP and 50 MP to further trace the variations.

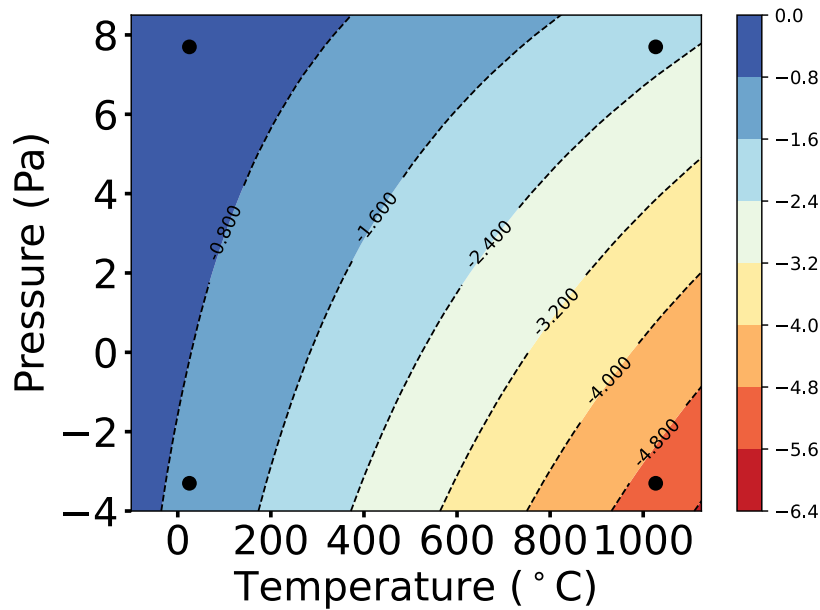


Figure S3: The contour plot of  $\Delta\mu_{\text{NH}_3}$ . The plot is derived from the equation (4). The black points is sampled the respective  $\Delta\mu_{\text{NH}_3}$ . (See Figure 8 of red, green, blue, and purple).



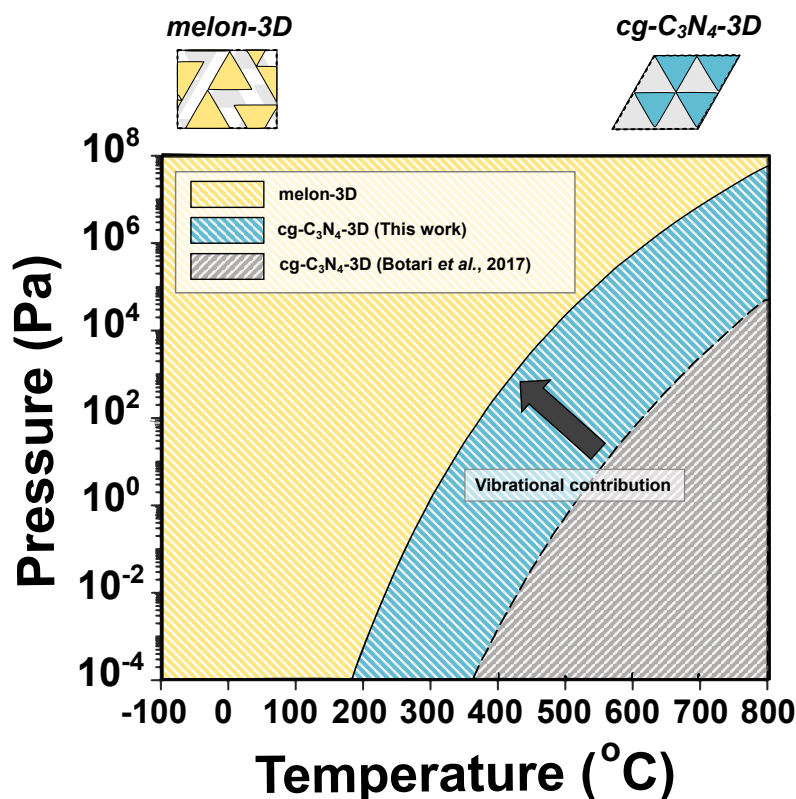


Figure S4: The calculated phase diagram of the normalized free energy of formation between melon-3D and  $\text{cg-C}_3\text{N}_4\text{-3D}$ . The inclusion of the vibrational contributions increases the relative stability of  $\text{cg-C}_3\text{N}_4\text{-3D}$  (blue area) to  $\Delta\mu_{\text{NH}_3}$  direction. The phase diagram of melon structure from the literature is shown in gray area.<sup>47</sup>

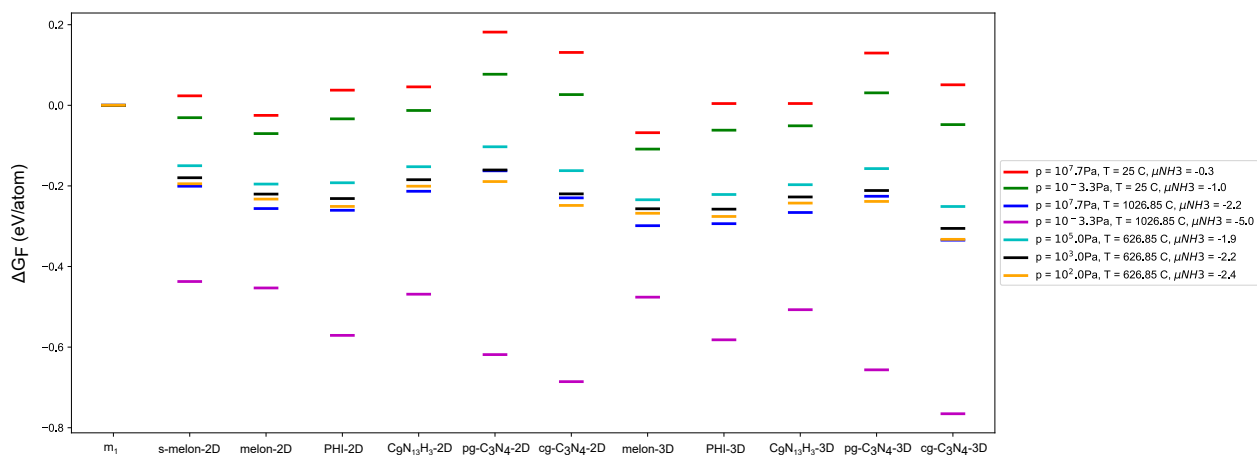


Figure S5: Free energy of formation for 2D and 3D structures with regards to various  $\mu_{\text{NH}_3}$ . The  $\mu_{\text{NH}_3}$  is differentiated from the combination of  $T$  and  $p_{\text{NH}_3}$ . The free energy of formation is normalized to eV/atom due to the different numbers of elements.

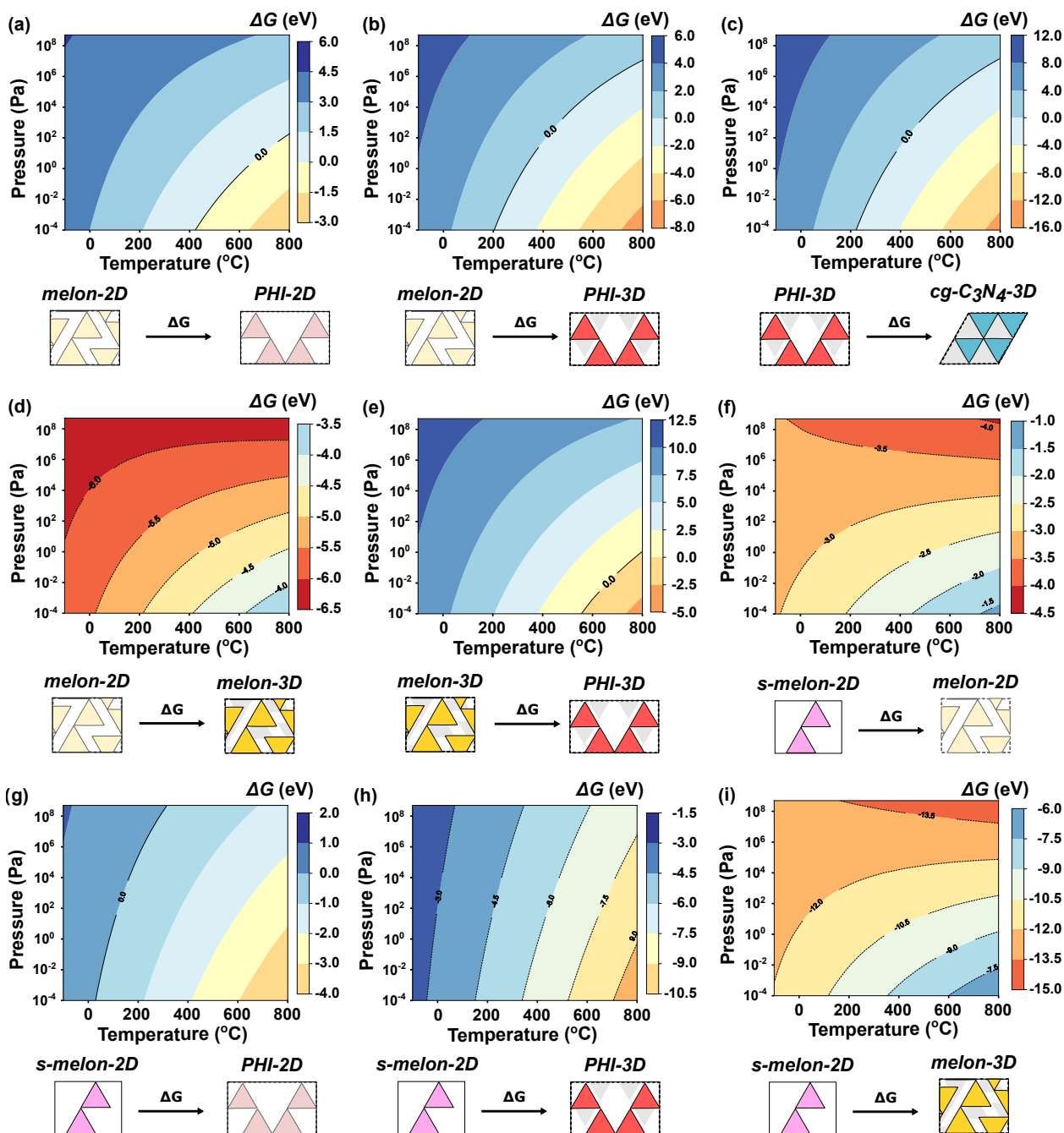


Figure S6: Respective phase diagram of the free energy reaction for 2D and 3D structures. The contour map is used to find spontaneous  $\Delta\mu_{\text{NH}_3}$  for temperature and  $p_{\text{NH}_3}$  conditions.

Table S1: Summary of Optical property

Structure	H-L gap (eV)	Structure	bandgap (eV)
h <sub>1</sub>	4.62	s-melon-2D	3.62
h <sub>2</sub>	3.98	melon-2D	3.68
h <sub>31</sub>	3.64	PHI-2D	3.32
h <sub>32</sub>	3.56	C <sub>9</sub> M <sub>13</sub> H <sub>3</sub> -2D	2.95
h <sub>33</sub>	3.92	cg-C <sub>3</sub> N <sub>4</sub> -2D	2.99
h <sub>34</sub>	3.80	pg-C <sub>3</sub> N <sub>4</sub> -2D	2.79
h <sub>41</sub>	3.52	s-melon-3D	3.39
h <sub>42</sub>	3.71	melon-3D	3.12
h <sub>43</sub>	3.52	PHI-3D	3.18
h <sub>44</sub>	3.61	C <sub>9</sub> M <sub>13</sub> H <sub>3</sub> -3D	2.86
h <sub>45</sub>	3.46	cg-C <sub>3</sub> N <sub>4</sub> -3D	2.95
h <sub>46</sub>	3.65	pg-C <sub>3</sub> N <sub>4</sub> -3D	2.35
h <sub>47</sub>	3.59	Mixed1-3D	2.95
h <sub>48</sub>	3.72	Mixed2-3D	2.88
		Mixed3-3D	2.99
		Mixed4-3D	2.89

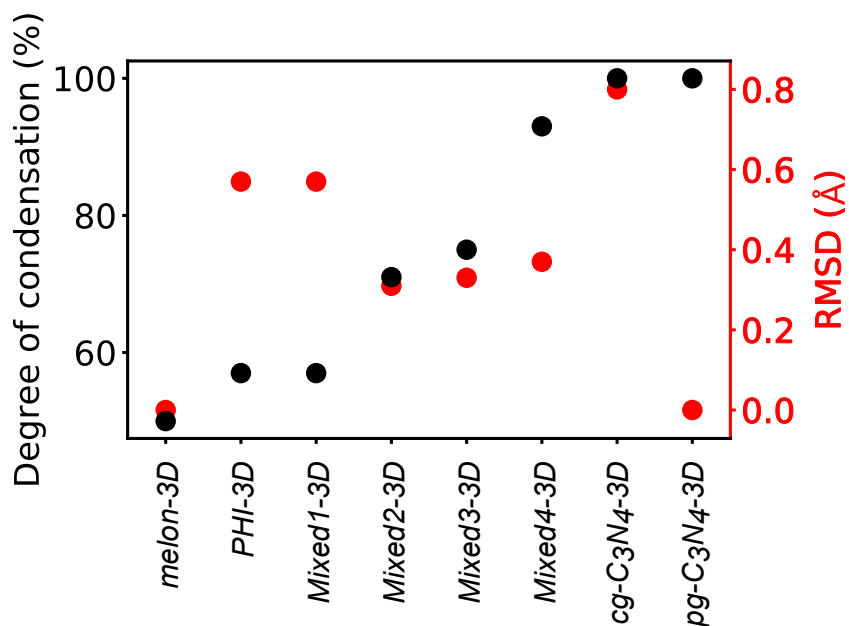


Figure S7: The degree of condensation and RMSD value are plotted with 3D structures. The Mixed structures are composed of PHI and g-C<sub>3</sub>N<sub>4</sub> structures (see Figure S1). The RMSD value of 3D structure is obtained from the average of the each layer.

Table S2: Summary of Degree of Corrugation

Structure	RMSD of out-of-plane (Å)	Structure	RMSD of out-of-plane (Å)
h <sub>1</sub>	0.01	melon-3D	0.00
h <sub>2</sub>	0.08	PHI-3D	0.33
h <sub>31</sub>	0.20	cg-C <sub>3</sub> N <sub>4</sub> -3D	0.80
h <sub>41</sub>	0.20	pg-C <sub>3</sub> N <sub>4</sub> -3D	0.00
h <sub>51</sub>	0.25	Mixed1-3D	0.57
Mixed1-2D	0.58	Mixed2-3D	0.57
Mixed3-2D	0.35	Mixed3-3D	0.31
PHI-2D	0.57	Mixed4-3D	0.37
cg-C <sub>3</sub> N <sub>4</sub> -2D	0.81		

## 7 Reference

### References

- (1) Kessler, F. K.; Zheng, Y.; Schwarz, D.; Merschjann, C.; Schnick, W.; Wang, X.; Boddys, M. J. Functional carbon nitride materials—design strategies for electrochemical devices. *Nature Reviews Materials* **2017**, *2*, 1–17.
- (2) Wang, X.; Maeda, K.; Chen, X.; Takahabe, K.; Domen, K.; Hou, Y.; Fu, X.; Antonietti, M. Polymer semiconductors for artificial photosynthesis: hydrogen evolution by mesoporous graphitic carbon nitride with visible light. *Journal of the American Chemical Society* **2009**, *131*, 1680–1681.
- (3) Schwinghammer, K.; Tuffy, B.; Mesch, M. B.; Wirnhier, E.; Martineau, C.; Taulelle, F.; Schnick, W.; Senker, J.; Lotsch, B. V. Triazine-based carbon nitrides for visible-light-driven hydrogen evolution. *Angewandte Chemie International Edition* **2013**, *52*, 2435–2439.
- (4) Liu, J.; Huang, J.; Zhou, H.; Antonietti, M. Uniform graphitic carbon nitride nanorod for efficient photocatalytic hydrogen evolution and sustained photoenzymatic catalysis. *ACS Applied Materials & Interfaces* **2014**, *6*, 8434–8440.

- (5) Savateev, A.; Antonietti, M. Ionic carbon nitrides in solar hydrogen production and organic synthesis: exciting chemistry and economic advantages. *ChemCatChem* **2019**, *11*, 6166–6176.
- (6) Zhang, G.; Li, G.; Heil, T.; Zafeiratos, S.; Lai, F.; Savateev, A.; Antonietti, M.; Wang, X. Tailoring the grain boundary chemistry of polymeric carbon nitride for enhanced solar hydrogen production and CO<sub>2</sub> reduction. *Angewandte Chemie International Edition* **2019**, *58*, 3433–3437.
- (7) Teixeira, I. F.; Tarakina, N. V.; Silva, I. F.; López-Salas, N.; Savateev, A.; Antonietti, M. Overcoming Electron Transfer Efficiency Bottlenecks for Hydrogen Production in Highly Crystalline Carbon Nitride-Based Materials. *Advanced Sustainable Systems* **2022**, 2100429.
- (8) Ding, Z.; Chen, X.; Antonietti, M.; Wang, X. Synthesis of transition metal-modified carbon nitride polymers for selective hydrocarbon oxidation. *ChemSusChem* **2011**, *4*, 274–281.
- (9) Zhang, J.; Grzelczak, M.; Hou, Y.; Maeda, K.; Domen, K.; Fu, X.; Antonietti, M.; Wang, X. Photocatalytic oxidation of water by polymeric carbon nitride nanohybrids made of sustainable elements. *Chemical Science* **2012**, *3*, 443–446.
- (10) Wang, C.; Wan, Q.; Cheng, J.; Lin, S.; Savateev, A.; Antonietti, M.; Wang, X. Efficient aerobic oxidation of alcohols to esters by acidified carbon nitride photocatalysts. *Journal of Catalysis* **2021**, *393*, 116–125.
- (11) da Silva, M. A.; Gil, J.; Tarakina, N. V.; Silva, G. T.; Balena, J.; Krambrock, K.; Antonietti, M.; Ribeiro, C.; Teixeira, I. Selective Methane Photooxidation into Methanol under Mild Conditions Promoted by Highly Dispersed Cu Atoms on Crystalline Carbon Nitrides. *Chemical Communications* **2022**,

- (12) Xia, P.; Antonietti, M.; Zhu, B.; Heil, T.; Yu, J.; Cao, S. Designing defective crystalline carbon nitride to enable selective CO<sub>2</sub> photoreduction in the gas phase. *Advanced Functional Materials* **2019**, *29*, 1900093.
- (13) Xia, Y.; Xiao, K.; Cheng, B.; Yu, J.; Jiang, L.; Antonietti, M.; Cao, S. Improving Artificial Photosynthesis over Carbon Nitride by Gas–Liquid–Solid Interface Management for Full Light-Induced CO<sub>2</sub> Reduction to C<sub>1</sub> and C<sub>2</sub> Fuels and O<sub>2</sub>. *ChemSusChem* **2020**, *13*, 1730–1734.
- (14) Lotsch, B. V.; Döblinger, M.; Sehnert, J.; Seyfarth, L.; Senker, J.; Oeckler, O.; Schnick, W. Unmasking melon by a complementary approach employing electron diffraction, solid-state NMR spectroscopy, and theoretical calculations—structural characterization of a carbon nitride polymer. *Chemistry—A European Journal* **2007**, *13*, 4969–4980.
- (15) Thomas, A.; Fischer, A.; Goettmann, F.; Antonietti, M.; Müller, J.-O.; Schlögl, R.; Carlsson, J. M. Graphitic carbon nitride materials: variation of structure and morphology and their use as metal-free catalysts. *Journal of Materials Chemistry* **2008**, *18*, 4893–4908.
- (16) Krivtsov, I.; Mitoraj, D.; Adler, C.; Ilkaeva, M.; Sardo, M.; Mafra, L.; Neumann, C.; Turchanin, A.; Li, C.; Dietzek, B., et al. Water-Soluble Polymeric Carbon Nitride Colloidal Nanoparticles for Highly Selective Quasi-Homogeneous Photocatalysis. *Angewandte Chemie International Edition* **2020**, *59*, 487–495.
- (17) Mitoraj, D.; Krivtsov, I.; Li, C.; Rajagopal, A.; Im, C.; Adler, C.; Köble, K.; Khainakova, O.; Hniopek, J.; Neumann, C., et al. A Study in Red: The Overlooked Role of Azo-Moieties in Polymeric Carbon Nitride Photocatalysts with Strongly Extended Optical Absorption. *Chemistry—A European Journal* **2021**, *27*, 17188–17202.
- (18) Lau, V. W.-h.; Lotsch, B. V. A Tour-Guide through Carbon Nitride-Land: Structure-

- and Dimensionality-Dependent Properties for Photo (Electro) Chemical Energy Conversion and Storage. *Advanced Energy Materials* **2022**, *12*, 2101078.
- (19) LIEBIG, J. Über einige Stickstoff - Verbindungen. *Annalen der Pharmacie* **1834**, *10*, 1–47.
- (20) Gmelin, L. Ueber einige Verbindungen des Melon's. *Annalen der Pharmacie* **1835**, *15*, 252–258.
- (21) Lotsch, B. V.; Schnick, W. Thermal conversion of guanlyurea dicyanamide into graphitic carbon nitride via prototype CN<sub>x</sub> precursors. *Chemistry of materials* **2005**, *17*, 3976–3982.
- (22) Lotsch, B. V.; Schnick, W. From triazines to heptazines: novel nonmetal tricyanome-laminates as precursors for graphitic carbon nitride materials. *Chemistry of materials* **2006**, *18*, 1891–1900.
- (23) Goettmann, F.; Fischer, A.; Antonietti, M.; Thomas, A. Chemical synthesis of meso-porous carbon nitrides using hard templates and their use as a metal-free catalyst for Friedel–Crafts reaction of benzene. *Angewandte Chemie International Edition* **2006**, *45*, 4467–4471.
- (24) Wang, X.; Maeda, K.; Thomas, A.; Takanabe, K.; Xin, G.; Carlsson, J. M.; Domen, K.; Antonietti, M. A metal-free polymeric photocatalyst for hydrogen production from water under visible light. *Nature materials* **2009**, *8*, 76–80.
- (25) Liu, A. Y.; Cohen, M. L. Prediction of new low compressibility solids. *Science* **1989**, *245*, 841–842.
- (26) Gracia, J.; Kroll, P. Corrugated layered heptazine-based carbon nitride: the lowest energy modifications of C<sub>3</sub>N<sub>4</sub> ground state. *Journal of Materials Chemistry* **2009**, *19*, 3013–3019.

- (27) Li, X.; Melissen, S. T.; Le Bahers, T.; Sautet, P.; Masters, A. F.; Steinmann, S. N.; Maschmeyer, T. Shining light on carbon nitrides: leveraging temperature to understand optical gap variations. *Chemistry of Materials* **2018**, *30*, 4253–4262.
- (28) Bojdys, M. J.; Müller, J.-O.; Antonietti, M.; Thomas, A. Ionothermal synthesis of crystalline, condensed, graphitic carbon nitride. *Chemistry—A European Journal* **2008**, *14*, 8177–8182.
- (29) Algara-Siller, G.; Severin, N.; Chong, S. Y.; Björkman, T.; Palgrave, R. G.; Laybourn, A.; Antonietti, M.; Khimyak, Y. Z.; Krashennnikov, A. V.; Rabe, J. P., et al. Triazine-based graphitic carbon nitride: a two-dimensional semiconductor. *Angewandte Chemie International Edition* **2014**, *53*, 7450–7455.
- (30) Lau, V. W.-h.; Moudrakovski, I.; Botari, T.; Weinberger, S.; Mesch, M. B.; Duppel, V.; Senker, J.; Blum, V.; Lotsch, B. V. Rational design of carbon nitride photocatalysts by identification of cyanamide defects as catalytically relevant sites. *Nature communications* **2016**, *7*, 1–10.
- (31) Melissen, S.; Le Bahers, T.; Steinmann, S. N.; Sautet, P. Relationship between carbon nitride structure and exciton binding energies: a DFT perspective. *The Journal of Physical Chemistry C* **2015**, *119*, 25188–25196.
- (32) Steinmann, S. N.; Melissen, S. T.; Le Bahers, T.; Sautet, P. Challenges in calculating the bandgap of triazine-based carbon nitride structures. *Journal of Materials Chemistry A* **2017**, *5*, 5115–5122.
- (33) Perdew, J. P. Density functional theory and the band gap problem. *International Journal of Quantum Chemistry* **1985**, *28*, 497–523.
- (34) Melissen, S.; Le Bahers, T.; Steinmann, S. N.; Sautet, P. Relationship between carbon nitride structure and exciton binding energies: a DFT perspective. *The Journal of Physical Chemistry C* **2015**, *119*, 25188–25196.



- (35) Melissen, S. T.; Steinmann, S. N.; Le Bahers, T.; Sautet, P. DFT perspective on the thermochemistry of carbon nitride synthesis. *The Journal of Physical Chemistry C* **2016**, *120*, 24542–24550.
- (36) Wei, W.; Jacob, T. Strong excitonic effects in the optical properties of graphitic carbon nitride g-C<sub>3</sub>N<sub>4</sub> from first principles. *Physical Review B* **2013**, *87*, 085202.
- (37) Godin, R.; Wang, Y.; Zwiijnenburg, M. A.; Tang, J.; Durrant, J. R. Time-resolved spectroscopic investigation of charge trapping in carbon nitrides photocatalysts for hydrogen generation. *Journal of the American Chemical Society* **2017**, *139*, 5216–5224.
- (38) Yang, W.; Godin, R.; Kasap, H.; Moss, B.; Dong, Y.; Hillman, S. A.; Steier, L.; Reiser, E.; Durrant, J. R. Electron accumulation induces efficiency bottleneck for hydrogen production in carbon nitride photocatalysts. *Journal of the American Chemical Society* **2019**, *141*, 11219–11229.
- (39) Li, C.; Hofmeister, E.; Krivtsov, I.; Mitoraj, D.; Adler, C.; Beranek, R.; Dietzek, B. Photodriven Charge Accumulation and Carrier Dynamics in a Water-Soluble Carbon Nitride Photocatalyst. *ChemSusChem* **2021**, *14*, 1728–1736.
- (40) Adler, C.; Selim, S.; Krivtsov, I.; Li, C.; Mitoraj, D.; Dietzek, B.; Durrant, J. R.; Beranek, R. Photodoping and Fast Charge Extraction in Ionic Carbon Nitride Photoanodes. *Advanced Functional Materials* **2021**, *31*, 2105369.
- (41) Seo, G.; Saito, Y.; Nakamichi, M.; Nakano, K.; Tajima, K.; Kanai, K. Mechanism of charge accumulation of poly (heptazine imide) gel. *Scientific reports* **2021**, *11*, 1–12.
- (42) Kröger, J.; Jiménez-Solano, A.; Savasci, G.; Rovó, P.; Moudrakovski, I.; Küster, K.; Schlomberg, H.; Vignolo-González, H. A.; Duppel, V.; Grunenber, L., et al. Interfacial engineering for improved photocatalysis in a charge storing 2D carbon nitride: melamine functionalized poly (heptazine imide). *Advanced Energy Materials* **2021**, *11*, 2003016.

- (43) Ruan, Z.-H.; Gao, X.-Y.; Yuan, Y.; Tan, H.-P. Theoretical insight into the effect of Br, Na co-doping on electronic structure, photocatalytic and optical characteristics of g-C<sub>3</sub>N<sub>4</sub> using first-principles and optical simulations. *Journal of Materials Science* **2021**, *56*, 10382–10392.
- (44) Dong, H.; Zuo, Y.; Song, N.; Hong, S.; Xiao, M.; Zhu, D.; Sun, J.; Chen, G.; Li, C. Bimetallic synergetic regulating effect on electronic structure in cobalt/vanadium co-doped carbon nitride for boosting photocatalytic performance. *Applied Catalysis B: Environmental* **2021**, *287*, 119954.
- (45) Cheng, L.; Zhang, H.; Li, X.; Fan, J.; Xiang, Q. Carbon–graphitic carbon nitride hybrids for heterogeneous photocatalysis. *Small* **2021**, *17*, 2005231.
- (46) Tang, J.-Y.; Er, C.-C.; Tan, L.-L.; Chew, Y.-H.; Mohamed, A. R.; Chai, S.-P. Uncovering the multifaceted roles of nitrogen defects in graphitic carbon nitride for selective photocatalytic carbon dioxide reduction: a density functional theory study. *Physical Chemistry Chemical Physics* **2022**, *24*, 11124–11130.
- (47) Botari, T.; Huhn, W. P.; Lau, V. W. H.; Lotsch, B. V.; Blum, V. Thermodynamic Equilibria in Carbon Nitride Photocatalyst Materials and Conditions for the Existence of Graphitic Carbon Nitride g-C<sub>3</sub>N<sub>4</sub>. *Chem. Mater.* **2017**, *29*, 4445–4453.
- (48) Kresse, G.; Hafner, J. Ab initio molecular dynamics for liquid metals. *Physical review B* **1993**, *47*, 558.
- (49) Kresse, G.; Hafner, J. Ab initio molecular-dynamics simulation of the liquid-metal–amorphous-semiconductor transition in germanium. *Physical Review B* **1994**, *49*, 14251.
- (50) Kresse, G.; Furthmüller, J. Efficiency of ab-initio total energy calculations for metals and semiconductors using a plane-wave basis set. *Computational materials science* **1996**, *6*, 15–50.

- (51) Kresse, G.; Furthmüller, J. Efficient iterative schemes for ab initio total-energy calculations using a plane-wave basis set. *Physical review B* **1996**, *54*, 11169.
- (52) Kresse, G.; Joubert, D. From ultrasoft pseudopotentials to the projector augmented-wave method. *Physical review b* **1999**, *59*, 1758.
- (53) Grimme, S.; Antony, J.; Ehrlich, S.; Krieg, H. A consistent and accurate ab initio parametrization of density functional dispersion correction (DFT-D) for the 94 elements H-Pu. *The Journal of chemical physics* **2010**, *132*, 154104.
- (54) Grimme, S.; Ehrlich, S.; Goerigk, L. Effect of the damping function in dispersion corrected density functional theory. *Journal of computational chemistry* **2011**, *32*, 1456–1465.
- (55) Perdew, J. P.; Burke, K.; Ernzerhof, M. Generalized gradient approximation made simple. *Physical review letters* **1996**, *77*, 3865.
- (56) Krukau, A. V.; Vydrov, O. A.; Izmaylov, A. F.; Scuseria, G. E. Influence of the exchange screening parameter on the performance of screened hybrid functionals. *The Journal of chemical physics* **2006**, *125*, 224106.
- (57) Neese, F. The ORCA program system. *Wiley Interdisciplinary Reviews: Computational Molecular Science* **2012**, *2*, 73–78.
- (58) Neese, F. Software update: the ORCA program system, version 4.0. *Wiley Interdisciplinary Reviews: Computational Molecular Science* **2018**, *8*, e1327.
- (59) Ernzerhof, M.; Scuseria, G. E. Assessment of the Perdew–Burke–Ernzerhof exchange–correlation functional. *The Journal of chemical physics* **1999**, *110*, 5029–5036.
- (60) Adamo, C.; Barone, V. Toward reliable density functional methods without adjustable parameters: The PBE0 model. *The Journal of chemical physics* **1999**, *110*, 6158–6170.

- (61) Monkhorst, H. J.; Pack, J. D. Special points for Brillouin-zone integrations. *Physical Review B* **1976**, *13*, 5188.
- (62) Togo, A.; Chaput, L.; Tanaka, I.; Hug, G. First-principles phonon calculations of thermal expansion in Ti<sub>3</sub>SiC<sub>2</sub>, Ti<sub>3</sub>AlC<sub>2</sub>, and Ti<sub>3</sub>GeC<sub>2</sub>. *Physical Review B* **2010**, *81*, 174301.
- (63) Chaput, L.; Togo, A.; Tanaka, I.; Hug, G. Phonon-phonon interactions in transition metals. *Physical Review B* **2011**, *84*, 094302.
- (64) Togo, A.; Tanaka, I. First principles phonon calculations in materials science. *Scripta Materialia* **2015**, *108*, 1–5.
- (65) Im, C.; Kirchhoff, B.; Krivtsov, I.; Mitoraj, D.; Beranek, R.; Jacob, T. Supporting Dataset for: Investigation of Thermochemical Relationship between Structural and Optical Properties on Photocatalytic Carbon Nitride Materials. 2022; <https://doi.org/10.5281/zenodo.6953396>.
- (66) Rogal, J.; Reuter, K. *Ab initio atomistic thermodynamics for surfaces: A primer*; 2006.
- (67) Dill, K. A.; Bromberg, S.; Stigter, D. *Molecular driving forces: statistical thermodynamics in biology, chemistry, physics, and nanoscience*; Garland Science, 2010.
- (68) Reuter, K. Ab initio thermodynamics and first-principles microkinetics for surface catalysis. *Catalysis Letters* **2016**, *146*, 541–563.
- (69) Gao, Q.; Zhuang, X.; Hu, S.; Hu, Z. Corrugation Matters: Structure Models of Single Layer Heptazine-Based Graphitic Carbon Nitride from First-Principles Studies. *The Journal of Physical Chemistry C* **2020**, *124*, 4644–4651.
- (70) Yan, S.; Li, Z.; Zou, Z. Photodegradation performance of g-C<sub>3</sub>N<sub>4</sub> fabricated by directly heating melamine. *Langmuir* **2009**, *25*, 10397–10401.

- (71) Lotsch, B. V.; Schnick, W. New light on an old story: formation of melam during thermal condensation of melamine. *Chemistry—A European Journal* **2007**, *13*, 4956–4968.
- (72) Dougherty, R. C. Temperature and pressure dependence of hydrogen bond strength: A perturbation molecular orbital approach. *The Journal of chemical physics* **1998**, *109*, 7372–7378.
- (73) Inoki, H.; Seo, G.; Kanai, K. Synthesis of graphitic carbon nitride under low ammonia partial pressure. *Applied Surface Science* **2020**, *534*, 147569.
- (74) Liu, J.; Wang, H.; Antonietti, M. Graphitic carbon nitride “reloaded”: emerging applications beyond (photo) catalysis. *Chemical Society Reviews* **2016**, *45*, 2308–2326.
- (75) Döblinger, M.; Lotsch, B. V.; Wack, J.; Thun, J.; Senker, J.; Schnick, W. Structure elucidation of polyheptazine imide by electron diffraction—a templated 2D carbon nitride network. *Chemical communications* **2009**, 1541–1543.
- (76) Dontsova, D.; Pronkin, S.; Wehle, M.; Chen, Z.; Fettkenhauer, C.; Clavel, G.; Antonietti, M. Triazoles: a new class of precursors for the synthesis of negatively charged carbon nitride derivatives. *Chemistry of Materials* **2015**, *27*, 5170–5179.
- (77) Savateev, A.; Pronkin, S.; Epping, J. D.; Willinger, M. G.; Wolff, C.; Neher, D.; Antonietti, M.; Dontsova, D. Potassium Poly (heptazine imides) from Aminotetrazoles: Shifting Band Gaps of Carbon Nitride-like Materials for More Efficient Solar Hydrogen and Oxygen Evolution. *ChemCatChem* **2017**, *9*, 167–174.
- (78) Chen, Z.; Savateev, A.; Pronkin, S.; Papaefthimiou, V.; Wolff, C.; Willinger, M. G.; Willinger, E.; Neher, D.; Antonietti, M.; Dontsova, D. “The easier the better” preparation of efficient photocatalysts—Metastable poly (heptazine imide) salts. *Advanced Materials* **2017**, *29*, 1700555.

- (79) Lin, L.; Ren, W.; Wang, C.; Asiri, A.; Zhang, J.; Wang, X. Crystalline carbon nitride semiconductors prepared at different temperatures for photocatalytic hydrogen production. *Applied Catalysis B: Environmental* **2018**, *231*, 234–241.
- (80) Schlomberg, H.; Kröger, J.; Savasci, G.; Terban, M. W.; Bette, S.; Moudrakovski, I.; Duppel, V.; Podjaski, F.; Siegel, R.; Senker, J., et al. Structural insights into poly (heptazine imides): A light-storing carbon nitride material for dark photocatalysis. *Chemistry of Materials* **2019**, *31*, 7478–7486.
- (81) Deifallah, M.; McMillan, P. F.; Cora, F. Electronic and structural properties of two-dimensional carbon nitride graphenes. *The Journal of Physical Chemistry C* **2008**, *112*, 5447–5453.
- (82) Savateev, A.; Pronkin, S.; Willinger, M. G.; Antonietti, M.; Dontsova, D. Towards organic zeolites and inclusion catalysts: Heptazine imide salts can exchange metal cations in the solid state. *Chemistry—An Asian Journal* **2017**, *12*, 1517–1522.
- (83) Schwarzer, A.; Saplinova, T.; Kroke, E. Tri-s-triazines (s-heptazines)—from a “mystery molecule” to industrially relevant carbon nitride materials. *Coordination Chemistry Reviews* **2013**, *257*, 2032–2062.
- (84) Chase, M. W.; (US), N. I. S. O. *NIST-JANAF thermochemical tables*; American Chemical Society Washington, DC, 1998; Vol. 9.
- (85) NIST-JANAF Table – Ammonia. <http://kinetics.nist.gov/janaf/html/H-083.html>, Accessed: 2021-04-30.
- (86) Haar, L.; Gallagher, J. S. Thermodynamic properties of ammonia. *Journal of Physical and Chemical Reference Data* **1978**, *7*, 635–792.

## Graphical TOC Entry

Some journals require a graphical entry for the Table of Contents. This should be laid out “print ready” so that the sizing of the text is correct.

Inside the tocentry environment, the font used is Helvetica 8 pt, as required by *Journal of the American Chemical Society*.

The surrounding frame is 9 cm by 3.5 cm, which is the maximum permitted for *Journal of the American Chemical Society* graphical table of content entries. The box will not resize if the content is too big: instead it will overflow the edge of the box.

This box and the associated title will always be printed on a separate page at the end of the document.